SIAM J. SCI. COMPUT.
Vol. 44, No. 3, pp. A1381–A1404

HIGH-ORDER CLOSE EVALUATION OF LAPLACE LAYER POTENTIALS: A DIFFERENTIAL GEOMETRIC APPROACH*

HAI ZHU† AND SHRAVAN VEERAPANENI†

Abstract. This paper presents a new approach for solving the close evaluation problem in three dimensions, commonly encountered while solving linear elliptic partial differential equations via potential theory. The goal is to evaluate layer potentials close to the boundary over which they are defined. The approach introduced here converts these nearly singular integrals on a patch of the boundary to a set of nonsingular line integrals on the patch boundary using the Stokes theorem on manifolds. A function approximation scheme based on harmonic polynomials is designed to express the integrand in a form that is suitable for applying the Stokes theorem. As long as the data—the boundary and the density function—is given in a high-order format, the double-layer potential and its derivatives can be evaluated with high-order accuracy using this scheme both on and off the boundary. In particular, we present numerical results demonstrating seventh-order convergence on a smooth, warped torus example achieving 10-digit accuracy in evaluating double-layer potential at targets that are arbitrarily close to the boundary.

Key words. potential theory, singular integrals, harmonic polynomials, exterior calculus, high-order methods

AMS subject classifications. 65R20, 41A55

DOI. 10.1137/21M1423051

1. Introduction.

In this paper, we describe a high-order accurate numerical algorithm for evaluating the double-layer potential (DLP) for Laplace equation given by

$$\mathcal{D}[\mu](\boldsymbol{r}') = \int_{\mathcal{M}} \frac{\partial G(\boldsymbol{r}' - \boldsymbol{r})}{\partial \boldsymbol{n}_{\boldsymbol{r}}} \mu(\boldsymbol{r})\, dS_{\boldsymbol{r}}, \tag{1}$$

where $G(\boldsymbol{r}' - \boldsymbol{r}) = 1/4\pi|\boldsymbol{r}' - \boldsymbol{r}|$ is Green's function for the Laplace equation, $\mu(\boldsymbol{r})$ is a density function, $\mathcal{M}$ is a closed two-dimensional manifold in $\mathbb{R}^3$, and $\boldsymbol{n}_{\boldsymbol{r}}$ is its normal. Layer potentials such as the DLP satisfy the underlying partial differential equation (PDE) by construction and are often employed in the mathematical analysis and numerical solution of PDEs [16]. Fast and accurate numerical schemes for (1) are fundamentally important owing to the ubiquity of the Laplace equation in sciences and engineering. Moreover, they serve as templates for other linear elliptic PDE solvers via potential theory.

In practical applications, one needs to evaluate (1) both on and off the surface $\mathcal{M}$. If the target $\boldsymbol{r}'$ is located far off the surface, a smooth quadrature rule designed for the given surface representation can be applied efficiently. However, the integrand in (1) becomes weakly singular for on-surface targets and nearly singular for targets located close to the surface. In both cases, specialized quadrature rules are necessary

*Submitted to the journal's Methods and Algorithms for Scientific Computing section May 27, 2021; accepted for publication (in revised form) January 31, 2022; published electronically May 31, 2022.

https://doi.org/10.1137/21M1423051

Funding: The authors acknowledge support from NSF under grants DMS-1719834, DMS-1454010, and DMS-2012424 and the Mcubed program at the University of Michigan. The work of the second author was also supported by the Flatiron Institute, a division of the Simons Foundation.

†Department of Mathematics, University of Michigan, Ann Arbor, MI 48109 USA (hszhu@umich.edu, shravan@umich.edu).

to achieve the desired order of accuracy. While the subject of developing high-order rules for weakly singular integrals is a classical one, nearly singular integration is an active area of research. For two-dimensional problems (where $\mathcal{M}$ is a curve on the plane), significant progress has been made on accurate evaluation schemes for nearly singular integrals; some recent works include [20, 7, 21, 1, 32] (also see references therein). In contrast, a fewer number of works exists for high-order close evaluation in the case of three-dimensional problems, owing to the complexity of handling a stronger kernel singularity over high-order surface meshes.

Synopsis of the new approach. Consider a subdomain $D \subset \mathcal{M}$. A surface integral on D can be converted into a line integral on ∂D using the Stokes theorem on manifolds as long as the integrand is an exact form [23]. Clearly, this condition is not necessarily satisfied in the case of DLP (1) for an arbitrary μ. The main idea here is that we can construct basis functions for approximating μ in D, which when multiplied by the kernel in (1) are exact forms. Thereby, when the target $\boldsymbol{r}'$ is close to D, we can apply this procedure to convert a nearly singular surface integral on D to a nonsingular line integral on ∂D (assuming $\boldsymbol{r}'$ is not close to ∂D). In this paper, we construct such basis functions using harmonic polynomials and quaternion algebra. The scheme is relatively insensitive to the underlying high-order surface discretization. Once the density function is expressed in our basis on D (e.g., *via* collocation), the layer potential evaluation is carried out in a similar fashion as a product integration scheme, with the caveat that some smooth line integrals on ∂D need to computed numerically in addition.

Related work. Here, we restrict our discussion to closely related recent works; a more extensive literature survey on singular and near-singular integration schemes can be found in [11, 19, 18]. In the first class of methods, the issue of close evaluation is overcome by exploiting the smoothness of DLP away from $\mathcal{M}$. In the quadrature-by-expansion (`QBX`) scheme, originally proposed in [3, 14], the DLP is approximated at centers away from $\mathcal{M}$ using high-order local expansions, which are valid at points closer to or on $\mathcal{M}$. Extension of `QBX` to three-dimensional problems was recently explored in [22, 29, 30]. A related algorithm is the `hedgehog` scheme of [18], which in turn is an extension of the earlier work by Ying, Biros, and Zorin [34]. Similar to `QBX`, `hedgehog` exploits the smoothness of (1) away from the boundary and evaluates it at carefully chosen "check" points along a line passing through the target located close to $\mathcal{M}$ and extrapolates the solution to the target.

Another popular class of methods are those based on singularity subtraction, wherein, the kernel in (1) is split into a singular part and a smooth part, with the action of the former treated analytically. While low-order variants are often used in practice for three-dimensional problems, high-order extension was presented in [12] for toroidal geometries. Recently, an alternative strategy, termed as harmonic density interpolation (HDI), is presented in [19] which focuses on the density instead of the kernel. It regularizes the kernel singularities by splitting the density into two parts: one whose convolution with the kernel can be treated analytically and the other whose derivatives vanish to prescribed order as the target $\boldsymbol{r}'$ approaches the source $\boldsymbol{r}$. Lastly, regularized kernel methods for three-dimensional close evaluation were also developed recently in [6, 25]; high-order accuracy is achieved by introducing correction terms to control the regularization error.

Our approach shares many of the desirable features of `QBX` and `hedgehog` schemes including, prominently, the ease of integration with fast algorithms such as the fast multipole method [10] since it does not modify the kernel and affects the local part evaluation only. On the other hand, the fact that all the computational variables

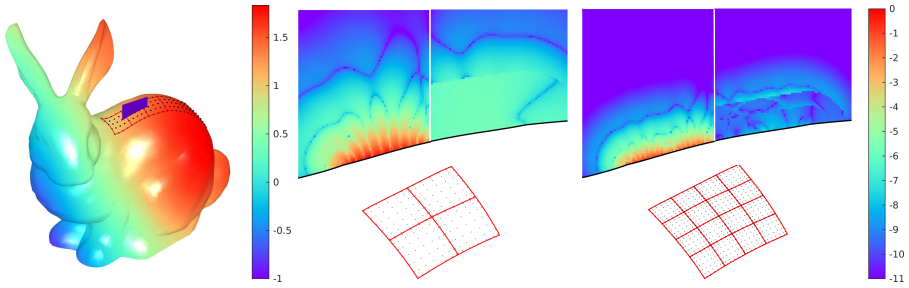

FIG. 1. *One of the key advantages of the close evaluation scheme developed in this paper is its ease of handling arbitrary meshes. Here, we demonstrate its performance on the Stanford bunny triangulation data* [27]. *We used the interactive sketch-based quadrangulation method of* [24] *to create high-quality quad remeshings locally as shown on the top of the bunny. We evaluate the DLP at targets that are located arbitrarily close to the surface as shown on top in blue color. The surface is colored by the density function* μ, *which was set as* $\mu(x, y, z) = e^{xy} - 1 + x + \sin(x^4 + 1/2y^3) + y - 1/2y^2 + 1/5y^6 + z$. *Middle and right: Given this setup, we demonstrate the performance of the new scheme by considering one of the quads, successively refining it twofold and visualizing the errors due to direct evaluation of DLP via the high-order smooth quadrature rule (left half) and the new close evaluation scheme (right half). We note that, while the errors stagnate in a band close to the surface in the case of smooth quadrature, the new scheme achieves uniform accuracy up to* 10 *digits. This is a self-convergence test compared with a reference solution obtained on an* 8×8 *panel refinement of the quad. More details on this experiment are provided in section* 5.

stay on the manifold $\mathcal{M}$ in our scheme offers further advantages such as avoiding the need for optimizing auxiliary parameters like local expansion centers or check points, which may be challenging in situations such as nearly self-touching geometries. Although both HDI and our scheme employ harmonic polynomials for approximating the density function, their usage is fundamentally different in both schemes. In [19], harmonic polynomial approximations are sought which cancel the kernel singularity to high-order as $\boldsymbol{r}' \to \boldsymbol{r}$; it is unclear if such approximations can be constructed to arbitrarily high-order in three-dimensions ([19] demonstrates third-order convergence). In contrast, our scheme only requires smoothness of the density. Lastly, a key advantage of our approach is that high-order convergence is guaranteed as long as the boundary mesh and the density function are specified in a high-order format (an example is shown in Figure 1).

In our view, our work is most closely related to the work of Helsing and Ojala [13], which developed a panel-based close evaluation scheme in two dimensions by approximating the density using monomial basis and evaluating their product with the nearly singular kernels via recurrences. This approach has been shown to offer a rapid and accurate solution of several elliptic problems [13, 5, 32]. The quaternionic harmonic polynomial approximation scheme of the density, introduced in this work, can be viewed as a three-dimensional analogue of their complex monomial approximation scheme. Similarly, we also employ recurrences to evaluate the product of nearly singular kernels and polynomial basis functions. We note that the differential geometry framework presented here is applicable both for two- and three-dimensional problems and, thereby, is a unifying approach.

Limitations. In this work, we restrict our attention to the Laplace layer potentials only. While our close evaluation scheme can be extended to other linear elliptic PDE kernels, it is by no means trivial: the density approximation scheme needs to be tailored for each individual kernel. We note, however, that there are alternative approaches to directly apply our scheme to other PDE problems—e.g., Stokes potentials

can be expressed as a linear combination of Laplace potentials and their derivatives [26]. Lastly, the method described in this paper cannot be applied directly to globally parameterized surfaces (e.g., spherical harmonic representations). One remedy is to maintain an auxiliary adaptive surface mesh just for the purposes of close evaluation.

The remainder of this paper is organized as follows. In section 2, we review some preliminaries on exterior calculus and describe the three-dimensional close evaluation problem using the language of exterior calculus. In section 3, the key ideas of the product integration scheme are outlined, followed by a presentation of our quaternionic approximation. Then in section 4, we present the overall implementation of our close evaluation scheme. We demonstrate the performance of our algorithm on a variety of examples in section 5, followed by conclusions and discussion on future directions in section 6.

2. Mathematical preliminaries. The use of exterior calculus greatly simplifies the presentation of our numerical algorithms even though, strictly speaking, it is not required for their development. In this section, we review some basic concepts but refer the reader to [2, 23] (or other standard textbooks) for a more thorough introduction to this subject.

2.1. Exterior algebra. If V is a vector space over $\mathbb{R}$, we will denote by $Alt^k(V)$ the space of alternating k-linear maps $V \times \ldots \times V \to \mathbb{R}$. We refer to such maps as alternating algebraic k-forms. A k-linear map $\omega \in Alt^k(V)$ is called alternating if

$$\omega(\boldsymbol{v}_1, \ldots, \boldsymbol{v}_i, \ldots, \boldsymbol{v}_j, \ldots, \boldsymbol{v}_k) = -\omega(\boldsymbol{v}_1, \ldots, \boldsymbol{v}_j, \ldots, \boldsymbol{v}_i, \ldots, \boldsymbol{v}_k). \tag{2}$$

Thus, an algebraic k-form on V assigns to a k-tuple $(\boldsymbol{v}_1, \ldots, \boldsymbol{v}_k)$ of elements of V a real number $\omega(\boldsymbol{v}_1, \ldots, \boldsymbol{v}_k)$, with the mapping linear in each argument, and reversing sign when any two arguments are interchanged.

Given $\omega \in Alt^k(V)$ and $\eta \in Alt^l(V)$, the simple tensor product of ω and η is usually not an alternating algebraic $(k+l)$-form. We instead employ the *exterior product* or *wedge product* $\omega \wedge \eta \in Alt^{k+l}$, defined by

$$\begin{aligned}(\omega \wedge \eta)(\boldsymbol{v}_1, \ldots, \boldsymbol{v}_{k+l}) \\ = \sum_{\sigma \in Sh_{k,l}} \operatorname{sgn}(\sigma) \omega(\boldsymbol{v}_{\sigma(1)}, \ldots, \boldsymbol{v}_{\sigma(k)}) \eta(\boldsymbol{v}_{\sigma(k+1)}, \ldots, \boldsymbol{v}_{\sigma(k+l)}), \quad \boldsymbol{v}_i \in V,\end{aligned} \tag{3}$$

where $Sh_{k,l}$ is the subset of (k,l) permutations of the set $\{1, 2, \ldots, k+l\}$ such that each element $\sigma \in Sh_{k,l}$ satisfies $\sigma(1) < \sigma(2) < \ldots < \sigma(k)$ and $\sigma(k+1) < \sigma(k+2) < \ldots < \ldots < \sigma(k+l)$. The exterior product is both bilinear and associative.

Throughout this paper, V will be $\mathbb{R}^3$, and k will be 1 or 2. In $\mathbb{R}^3$, the canonical basis $\boldsymbol{e}_1, \boldsymbol{e}_2$, and $\boldsymbol{e}_3$ gives rise to a natural dual basis of $Alt^1(\mathbb{R}^3)$, the space of covectors. This dual basis will often be denoted by dx, dy, and dz. These basis elements are linear maps (not to be confused with infinitely small change in the variable). For example, $dx(\boldsymbol{v}) = \boldsymbol{e}_1 \cdot \boldsymbol{v} = v_1$. The wedge product is also an operation connecting the various $Alt^k(V)$ spaces. For example, the basis for $Alt^2(\mathbb{R}^3)$ can be written using wedge products of $Alt^1(\mathbb{R}^3)$ basis elements as $dx \wedge dy, dy \wedge dz$, and $dz \wedge dx$.

2.2. Exterior calculus on manifolds. At each point $\boldsymbol{r}$ of a sufficiently smooth manifold $\mathcal{M}$ of dimension n, the tangent space $T_{\boldsymbol{r}}\mathcal{M}$ is a vector space of dimension n (in our case, $n = 2$). We could think of this as a local coordinate system. If the selection of a vector $\boldsymbol{v}(\boldsymbol{r})$ at $\boldsymbol{r}$ is made in each $T_{\boldsymbol{r}}\mathcal{M}$, we obtain a vector field.

Applying the exterior algebra construction to the tangent spaces, we obtain the exterior forms bundle $(\boldsymbol{r}, \eta)$ with $\boldsymbol{r} \in \mathcal{M}$, $\eta \in Alt^k(T_{\boldsymbol{r}}\mathcal{M})$. A differential k-form is

a map ω which associates to each $\boldsymbol{r} \in \mathcal{M}$ an element $\omega_{\boldsymbol{r}} \in Alt^k(T_{\boldsymbol{r}}\mathcal{M})$. If the map $\boldsymbol{r} \in \mathcal{M} \to \omega_{\boldsymbol{r}}(\boldsymbol{v}_1(\boldsymbol{r}), \ldots, \boldsymbol{v}_k(\boldsymbol{r})) \in \mathbb{R}$ is smooth whenever the $\boldsymbol{v}_i$'s are smooth vector fields, then we say that ω is a smooth differential k-form. We denote by $\Lambda^k(\mathcal{M})$ the space of all smooth differential k-forms on $\mathcal{M}$. As $\boldsymbol{r}$ moves around smoothly on $\mathcal{M}$, ω provides a smoothly varying algebraic k-form at each tangent space $T_{\boldsymbol{r}}\mathcal{M}$.

The exterior product of differential forms can be defined pointwise from the exterior product of algebraic forms:

$$(\omega \wedge \eta)_{\boldsymbol{r}} = \omega_{\boldsymbol{r}} \wedge \eta_{\boldsymbol{r}}. \tag{4}$$

If D is an oriented submanifold of $\mathcal{M}$ and ω is a continuous k-form, then the integral $\int_D \omega$ is well defined.

The exterior derivative d is a linear operator that maps $\Lambda^k(\mathcal{M})$ into $\Lambda^{k+1}(\mathcal{M})$ for each $k \geq 0$. We give a formula for the case $\mathcal{M}$ is a domain in $\mathbb{R}^n$. For given $\omega \in \Lambda^k(\mathcal{M})$ and vectors $\boldsymbol{v}_1, \ldots, \boldsymbol{v}_k$, we obtain a smooth mapping $\mathcal{M} \to \mathbb{R}$ given by $\boldsymbol{r} \to \omega_{\boldsymbol{r}}(\boldsymbol{v}_1, \ldots, \boldsymbol{v}_k)$. We then define

$$d\omega_{\boldsymbol{r}}(\boldsymbol{v}_1, \ldots, \boldsymbol{v}_k) = \sum_{j=1}^{k+1} (-1)^{j+1} \partial_{\boldsymbol{v}_j} \omega_{\boldsymbol{r}}(\boldsymbol{v}_1, \ldots, \hat{\boldsymbol{v}}_j, \ldots, \boldsymbol{v}_{k+1}), \tag{5}$$

where the hat is used to indicate a suppressed argument. If $\omega \in \Lambda^k(\mathcal{M})$ and $\eta \in \Lambda^l(\mathcal{M})$, then

$$d(\omega \wedge \eta) = d\omega \wedge \eta + (-1)^k \omega \wedge d\eta. \tag{6}$$

2.3. Integral equation formulation. Consider the following interior Dirichlet problem for the Laplace equation in a three-dimensional domain $\mathbb{D}$ bounded by $\mathcal{M}$:

$$\Delta u = 0 \quad \text{in} \quad \mathbb{D}, \quad u = g \quad \text{on} \quad \mathcal{M}. \tag{7}$$

We can employ an indirect integral equation formulation [16] for solving this problem, wherein we set $u(\boldsymbol{r}') = \mathcal{D}[\mu](\boldsymbol{r}')$, the DLP as defined in (1). This ansatz satisfies the Laplace equation by construction, and enforcing the boundary condition yields the following boundary integral equation (BIE) for the unknown μ:

$$-\frac{1}{2}\mu(\boldsymbol{r}') + \mathcal{D}[\mu](\boldsymbol{r}') = g(\boldsymbol{r}') \quad \text{for all} \quad \boldsymbol{r}' \in \mathcal{M}, \tag{8}$$

where the evaluation of $\mathcal{D}$ on $\mathcal{M}$ is performed in the principal value sense. Solving this BIE for μ, one can evaluate the solution u at any target in the domain by using (1). Similarly, other Laplace boundary value problems can be recast as BIEs using potential theory (e.g., see [16]).

Now, let us express the DLP evaluation as integration of differential forms. On the manifold $\mathcal{M}$, we have [23, Thm. 5–6]:

$$n_1\, dS_{\boldsymbol{r}} = dy \wedge dz, \quad n_2\, dS_{\boldsymbol{r}} = dz \wedge dx, \quad n_3\, dS_{\boldsymbol{r}} = dx \wedge dy. \tag{9}$$

Therefore, the DLP (1) can be written as

$$\begin{aligned} \mathcal{D}[\mu](\boldsymbol{r}') &= \int_{\mathcal{M}} \frac{(\boldsymbol{r}' - \boldsymbol{r}) \cdot \boldsymbol{n}_{\boldsymbol{r}}}{4\pi |\boldsymbol{r}' - \boldsymbol{r}|^3} \mu(\boldsymbol{r})\, dS_{\boldsymbol{r}} \\ &= \int_{\mathcal{M}} \frac{(x' - x)\mu(\boldsymbol{r})}{4\pi |\boldsymbol{r}' - \boldsymbol{r}|^3} dy \wedge dz + \frac{(y' - y)\mu(\boldsymbol{r})}{4\pi |\boldsymbol{r}' - \boldsymbol{r}|^3} dz \wedge dx + \frac{(z' - z)\mu(\boldsymbol{r})}{4\pi |\boldsymbol{r}' - \boldsymbol{r}|^3} dx \wedge dy, \end{aligned} \tag{10}$$

where $\boldsymbol{r}' = (x', y', z')$ and $\boldsymbol{r} = (x, y, z)$.

3. Density approximation and exact form construction. In this section, we systematically introduce the key ideas required to develop our numerical scheme. We provide the necessary analytical and algebraic background employed in section 4. We briefly review Stokes' theorem and Poincaré's lemma to illustrate our basic ideas in section 3.1 and introduce a quaternionic approximation scheme in section 3.2.

3.1. Stokes' theorem and Poincaré's lemma. We will be relying on the Stokes theorem to evaluate (10) when $\boldsymbol{r}'$ is close to $\mathcal{M}$. Using exterior calculus, one can summarize the Stokes theorem on a patch D in an elegant way [23].

THEOREM 3.1 (Stokes' theorem). *If D is a compact oriented 2-manifold, for any smooth 1-form ω defined on D, the following holds:*

$$\int_D d\omega = \int_{\partial D} \omega. \tag{11}$$

Remark 3.2. The advantage of using Stokes' theorem to reduce a surface integral of 2-form $d\omega$ on D to a line integral of 1-form ω is essentially twofold. One is that we have localized the work involved in evaluating layer potential on part of the integration surface. The other comes from the benefit of dimensionality reduction. Essentially, this eliminates singularity that populates the two-dimensional manifold to only boundaries of its panel discretization, which has a measure zero. This further helps in accurate evaluation of layer potentials when targets are extremely close to or on the surface.

The key idea is to use Stokes theorem to evaluate the DLP when a target $\boldsymbol{r}'$ is close to D. But Stokes' theorem does not help with finding a suitable ω such that

$$\begin{aligned}\frac{(\boldsymbol{r}'-\boldsymbol{r})\cdot\boldsymbol{n}_{\boldsymbol{r}}}{4\pi|\boldsymbol{r}'-\boldsymbol{r}|^3}\mu(\boldsymbol{r})\,dS_{\boldsymbol{r}} &= \frac{(x'-x)\mu(\boldsymbol{r})}{4\pi|\boldsymbol{r}'-\boldsymbol{r}|^3}dy\wedge dz + \frac{(y'-y)\mu(\boldsymbol{r})}{4\pi|\boldsymbol{r}'-\boldsymbol{r}|^3}dz\wedge dx \\ &\quad + \frac{(z'-z)\mu(\boldsymbol{r})}{4\pi|\boldsymbol{r}'-\boldsymbol{r}|^3}dx\wedge dy \approx d\omega.\end{aligned} \tag{12}$$

To address the challenges in systematically finding ω, we introduce one additional tool in differential geometry, Poincaré's lemma [23, Thm. 4–11]: for every differential form on an open star-shaped subset D of $\mathbb{R}^n$, suppose $d\alpha = 0$ for $\alpha \in \Lambda^k(D)$; then locally α is exact; i.e., there is some $\omega \in \Lambda^{k-1}(D)$ such that $d\omega = \alpha$. The proof of the lemma considers a $k-$form,

$$\alpha = \sum_{i_1<\cdots<i_k} g_{i_1,\ldots,i_k} dx^{i_1}\wedge\cdots\wedge dx^{i_k}, \tag{13}$$

and shows that $(k-1)$-form ω defined by

$$\omega = \sum_{i_1<\cdots<i_k}\sum_{l=1}^{k}(-1)^{(l-1)}\left(\int_0^1 t^{k-1} g_{i_1,\ldots,i_k}(t\boldsymbol{x})dt\right) x^{i_l}\, dx^{i_1}\wedge\cdots\wedge\hat{dx^{i_l}}\wedge\cdots\wedge dx^{i_k} \tag{14}$$

satisfies $d\omega = \alpha$ given $d\alpha = 0$.

Based on this result, we can accomplish the 2-to-1 form conversion as written in (12). This construction process can be viewed as finding the vector potential whose curl is a given vector field.

A simplified version of the Poincaré's lemma relevant to our setting can be summarized as follows.

LEMMA 3.3 (2-to-1 form conversion). *Consider a compact oriented two-dimensional manifold D in $\mathbb{R}^3$. Let*

$$\alpha = g_1(\boldsymbol{r})dy \wedge dz + g_2(\boldsymbol{r})dz \wedge dx + g_3(\boldsymbol{r})dx \wedge dy \tag{15}$$

be a differential 2-form on D. If $d\alpha = 0$ (i.e., $\nabla \cdot (g_1, g_2, g_3) = 0$), then α is an exact form on D; i.e., there exists some 1-form ω such that $d\omega = \alpha$. In particular, there is an explicit construction:

$$\begin{aligned}\omega = &\left(\int_0^1 (tzg_2(t\boldsymbol{r}) - tyg_3(t\boldsymbol{r}))\, dt\right) dx + \left(\int_0^1 (txg_3(t\boldsymbol{r}) - tzg_1(t\boldsymbol{r}))\, dt\right) dy \\ &+ \left(\int_0^1 (tyg_1(t\boldsymbol{r}) - txg_2(t\boldsymbol{r}))\, dt\right) dz.\end{aligned} \tag{16}$$

Proof. See Appendix A ∎

Consequently, it is possible to convert a surface integral into a line integral as long as the vector $\boldsymbol{g}$ is divergence-free. For example, if μ is a scalar in (12), it is clear that the above lemma applies since

$$\nabla \cdot \frac{\boldsymbol{r}' - \boldsymbol{r}}{|\boldsymbol{r}' - \boldsymbol{r}|^3} = \nabla \cdot \nabla \frac{1}{|\boldsymbol{r}' - \boldsymbol{r}|} = -\delta(\boldsymbol{r}', \boldsymbol{r}),$$

where $\delta(\boldsymbol{r}', \boldsymbol{r})$ is the Dirac δ function. Therefore $\nabla \cdot \frac{\boldsymbol{r}'-\boldsymbol{r}}{|\boldsymbol{r}'-\boldsymbol{r}|^3} = 0$ for $\boldsymbol{r}' \neq \boldsymbol{r}$. In the general case, our goal is to find a high-order approximation scheme for μ which makes the vector $(\boldsymbol{r}' - \boldsymbol{r})\mu(\boldsymbol{r})/|\boldsymbol{r}' - \boldsymbol{r}|^3$ divergence-free. Clearly, standard polynomial approximation schemes (e.g., tensor-product monic polynomials) will not yield the desired result. In the next subsection, we present an approximation scheme based on harmonic polynomials and quaternionic representations that accomplishes this task.

The key insight that motivates our approach is summarized in Lemma 3.4, but first let us review some preliminaries on quaternions. Let $\boldsymbol{i}, \boldsymbol{j}$, and $\boldsymbol{k}$ be the standard quaternion units; that is, they satisfy the identities

$$\boldsymbol{i}^2 = \boldsymbol{j}^2 = \boldsymbol{k}^2 = \boldsymbol{ijk} = -1, \quad \boldsymbol{ij} = \boldsymbol{k} = -\boldsymbol{ji}, \quad \boldsymbol{jk} = \boldsymbol{i} = -\boldsymbol{kj}, \quad \boldsymbol{ki} = \boldsymbol{j} = -\boldsymbol{ik}. \tag{17}$$

A quaternionic function g is comprised of a scalar part g_0 and a vector part $\boldsymbol{g} = (g_1, g_2, g_3)$ and written as

$$g(\boldsymbol{r}) = g_0(\boldsymbol{r}) + g_1(\boldsymbol{r})\boldsymbol{i} + g_2(\boldsymbol{r})\boldsymbol{j} + g_3(\boldsymbol{r})\boldsymbol{k}.$$

Alternatively, one can write the quaternion in the pair form as $g = (g_0, \boldsymbol{g})$. For any given vector $\boldsymbol{g}$, we can define a quaternion g as above, and if not specified, $g_0 = 0$ is assumed by default. Using (17), we can easily verify the product of two quaternions g and h, denoted in the pair form, to be

$$f = gh = (g_0h_0 - \boldsymbol{g} \cdot \boldsymbol{h},\, g_0\boldsymbol{h} + h_0\boldsymbol{g} + \boldsymbol{g} \times \boldsymbol{h}) = (f_0, \boldsymbol{f}),$$

where the scalar entry $f_0 = g_0h_0 - \boldsymbol{g} \cdot \boldsymbol{h}$ is not necessarily 0 and the vector entry $g_0\boldsymbol{h} + h_0\boldsymbol{g} + \boldsymbol{g} \times \boldsymbol{h}$ is $\boldsymbol{f}$. With these preliminaries, we can now state and prove the following lemma that motivates our density approximation scheme.

LEMMA 3.4. *Let $\boldsymbol{g} = \nabla\psi$ and $\boldsymbol{f} = \nabla\phi$, where ϕ and ψ are some harmonic functions. Then each component of the quaternionic 2-form $gn_rf\, dS_{\boldsymbol{r}}$ is exact, where g, n_r, and f are quaternions corresponding to $\boldsymbol{g}$, $\boldsymbol{n_r}$, and $\boldsymbol{f}$.*

Proof. Using the identities (17), after some algebra, we obtain

$$gn_r f = (-(\boldsymbol{g} \times \boldsymbol{n_r}) \cdot \boldsymbol{f}, -(\boldsymbol{g} \cdot \boldsymbol{n_r})\, \boldsymbol{f} + (\boldsymbol{g} \times \boldsymbol{n_r}) \times \boldsymbol{f})\,.$$

The scalar part of $gn_r f\, dS_{\boldsymbol{r}}$ then becomes

$$-(\boldsymbol{g} \times \boldsymbol{n_r}) \cdot \boldsymbol{f}\, dS_{\boldsymbol{r}} = -(\boldsymbol{f} \times \boldsymbol{g}) \cdot \boldsymbol{n_r}\, dS_{\boldsymbol{r}}.$$

Invoking the fact that both $\boldsymbol{g}$ and $\boldsymbol{f}$ are gradients of harmonic functions, we get

$$\nabla \cdot (\boldsymbol{f} \times \boldsymbol{g}) = \boldsymbol{g} \cdot (\nabla \times \nabla \phi) - \boldsymbol{f} \cdot (\nabla \times \nabla \psi) = 0,$$

thereby confirming that the scalar part is an exact form (using Lemma 3.3). Similarly, the first component of its vector part is given by

$$(n_1 (\boldsymbol{g} \cdot \boldsymbol{f}) - g_1 (\boldsymbol{f} \cdot \boldsymbol{n_r}) - f_1 (\boldsymbol{g} \cdot \boldsymbol{n_r}))\, dS_{\boldsymbol{r}} = ((\boldsymbol{g} \cdot \boldsymbol{f})\, \boldsymbol{e}_1 - g_1 \boldsymbol{f} - f_1 \boldsymbol{g}) \cdot \boldsymbol{n_r}\, dS_{\boldsymbol{r}}.$$

Therefore, this term is also exact since

$$\nabla \cdot ((\boldsymbol{g} \cdot \boldsymbol{f})\, \boldsymbol{e}_1 - g_1 \boldsymbol{f} - f_1 \boldsymbol{g}) = \frac{\partial}{\partial x} (\boldsymbol{g} \cdot \boldsymbol{f}) - \nabla g_1 \cdot \boldsymbol{f} - g_1 \Delta \phi - \nabla f_1 \cdot \boldsymbol{g} - f_1 \Delta \psi = 0.$$

∎

The following corollary applies this lemma to help verify the divergence-free condition in Lemma 3.3 to convert the double-layer integral into a 1-form integral.

COROLLARY 3.5. *Let α be a quaternionic differential 2-form on D given by*

$$\alpha = \alpha_0 + \alpha_1 \boldsymbol{i} + \alpha_2 \boldsymbol{j} + \alpha_3 \boldsymbol{k} = \frac{(r' - r) n_r}{|r' - r|^3} f(\boldsymbol{r})\, dS_{\boldsymbol{r}}, \tag{18}$$

where r', r, n_r, and f are quaternions corresponding to $\boldsymbol{r}'$, $\boldsymbol{r}$, $\boldsymbol{n_r}$, and $\boldsymbol{f}$. If the vector $\boldsymbol{f}(\boldsymbol{r})$ is the gradient of a harmonic function, then $d\alpha_i = 0$, $i = 0, 1, 2, 3$.

Proof. This result directly follows from Lemma 3.4 by setting $\boldsymbol{g}(\boldsymbol{r}) = \nabla \frac{1}{|\boldsymbol{r}' - \boldsymbol{r}|}$ and noting that $|r' - r| = |\boldsymbol{r}' - \boldsymbol{r}|$. ∎

3.2. Approximation scheme using harmonic polynomials and quaternionic representation. Our goal is to express the density μ in terms of some basis functions that allow us to apply Corollary 3.5 to convert the DLP (10) to a 1-form using Lemma 3.3. From Corollary 3.5, it is clear that the elements of such a basis set essentially must be in quaternionic form and their vector components must be gradients of some harmonic functions (notice that in Corollary 3.5 we need to expand the quaternionic form $\frac{(r' - r) n_r}{|r' - r|^3} f(\boldsymbol{r})\, dS_{\boldsymbol{r}}$ before projecting the surface elements). To construct such a basis set, we turn to *harmonic polynomials*, which are homogeneous polynomials that satisfy the Laplace equation (we refer the reader to [8] for a review on this topic).

While there are $2p + 1$ independent harmonic polynomials of degree p, we will chose p of them for our construction. The only requirement is that their gradients must be linearly independent. We use, for example, the following set of harmonic

polynomials for up to degree 7:

$$
\begin{aligned}
\mathcal{P}_1 =&\{z\},\ \mathcal{P}_2 = \{x^2 - z^2,\ y^2 - z^2\},\ \mathcal{P}_3 = \{x^3 - 3xz^2,\ y^3 - 3yz^2,\ xyz\},\\
\mathcal{P}_4 =&\{x^4 - 6x^2z^2 + z^4,\ y^4 - 6y^2z^2 + z^4, 3x^2yz - yz^3,\ 3xy^2z - xz^3\},\\
\mathcal{P}_5 =&\{x^5 - 10x^3z^2 + 5xz^4,\ y^5 - 10y^3z^2 + 5yz^4,\ x^4y - 6x^2yz^2 + yz^4,\\
&\quad xy^4 - 6xy^2z^2 + xz^4,\ -15x^2y^2z + 5x^2z^3 + 5y^2z^3 - z^5\},\\
\mathcal{P}_6 =&\{x^6 - 15x^4z^2 + 15x^2z^4 - z^6,\ y^6 - 15y^4z^2 + 15y^2z^4 - z^6,\\
&\quad x^5y - 10x^3yz^2 + 5xyz^4,\ xy^5 - 10xy^3z^2 + 5xyz^4,\\
&\quad 5x^4yz - 10x^2y^3z + y^5z,\ 5xy^4z - 10x^3y^2z + x^5z\},\\
\mathcal{P}_7 =&\{x^7 - 7xz^6 + 35x^3z^4 - 21x^5z^2,\ y^7 - 7yz^6 + 35y^3z^4 - 21y^5z^2,\\
&\quad x^6y - 15x^4yz^2 + 15x^2yz^4 - z^6y,\ xy^6 - 15xy^4z^2 + 15xy^2z^4 - xz^6,\\
&\quad 3x^5y^2 - 3x^5z^2 - 30x^3y^2z^2 + 10x^3z^4 + 15xy^2z^4 - 3xz^6,\\
&\quad 3x^2y^5 - 3y^5z^2 - 30x^2y^3z^2 + 15x^2yz^4 + 10y^3z^4 - 3yz^6,\\
&\quad (3x^5y - 10x^3y^3 + 3xy^5)z\}.
\end{aligned}
\tag{19}
$$

Then, we assign the gradients of each of these harmonic polynomials, expressed in quaternionic form, as the elements of the required basis set. Denoting this set by $\{f^{(k,1)}, \ldots, f^{(k,k)}\}, k = 1, \ldots, p$, we can easily derive them from (19) as

$$
\begin{aligned}
&\nabla\mathcal{P}_1 = \{f^{(1,1)} = \boldsymbol{k}\}, \quad \nabla\mathcal{P}_2 = \{f^{(2,1)} = x\boldsymbol{i} - z\boldsymbol{k},\ f^{(2,2)} = y\boldsymbol{j} - z\boldsymbol{k}\},\\
&\nabla\mathcal{P}_3 = \{f^{(3,1)} = \left(x^2 - z^2\right)\boldsymbol{i} - 2xz\boldsymbol{k},\ f^{(3,2)} = \left(y^2 - z^2\right)\boldsymbol{j} - 2yz\boldsymbol{k},\\
&\qquad f^{(3,3)} = yz\boldsymbol{i} + xz\boldsymbol{j} + xy\boldsymbol{k}\},
\end{aligned}
\tag{20}
$$

and so on. Therefore, in total, there are $p(p+1)/2$ quaternionic functions in this basis set. Moreover, the set $\nabla\mathcal{P}_p$ is composed of homogeneous, quaternionic polynomials of degree $(p-1)$. Thereby, a pth-order convergent scheme is obtained when the set $\{\nabla\mathcal{P}_k,\ k = 1, \ldots, p\}$ is used for approximating smooth quaternionic functions.

Now, consider a triangular patch $D \subset \mathcal{M}$, as illustrated in Figure 2(b). On this patch, we use the basis functions $\{f^{(k,l)}(\boldsymbol{r})\}$ to approximate the density function as

$$
\mu(\boldsymbol{r}) + 0\boldsymbol{i} + 0\boldsymbol{j} + 0\boldsymbol{k} \approx \sum_{k=1}^{p}\sum_{l=1}^{k} f^{(k,l)}(\boldsymbol{r})\, c^{(k,l)},
\tag{21}
$$

where the unknown coefficients $c^{(k,l)}$ are also quaternions, that is,

$$
c^{(k,l)} = c_0^{(k,l)} + c_1^{(k,l)}\boldsymbol{i} + c_2^{(k,l)}\boldsymbol{j} + c_3^{(k,l)}\boldsymbol{k}.
$$

Therefore, there are $4 \cdot \frac{p(p+1)}{2}$ unknowns that need to be determined. They can be obtained, for instance, by applying a standard collocation scheme. For a p-node composite tensor-product Gauss–Legendre quadrature in Figure 2(c), there are $(p^2 + p)/2$ quadrature nodes on the preimage of each triangular patch D, denoted as $\{\boldsymbol{r}^{(k,l)} | 1 \le k \le l \le p\}$. Enforcing (21) at these quadrature nodes will generate the required $4 \cdot \frac{p(p+1)}{2}$ number of equations. Empirically, we found that the resulting square linear systems are invertible in general.

Remark 3.6. In our implementation, we perform a change of coordinates in each patch so that $\boldsymbol{r}^{(1,1)}$ becomes the origin (as illustrated in Figure 2(c)). In this case,

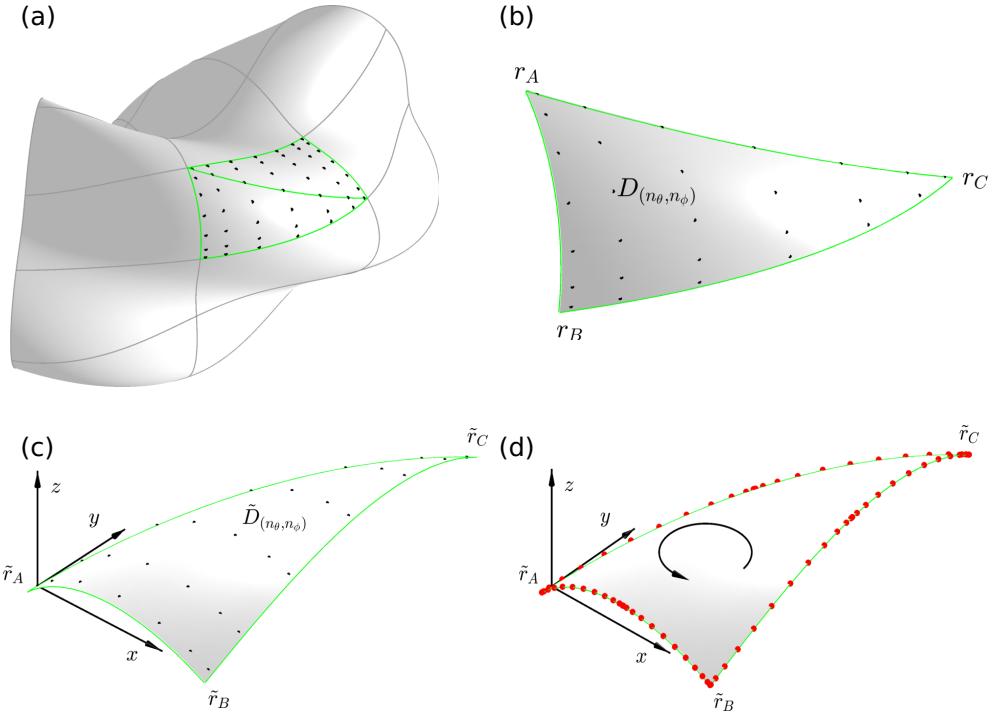

FIG. 2. *Schematic of our proposed product integration scheme for Laplace DLP.* (a) *is part of a parametrized "cruller" surface.* (b) *is one of the triangular subpanel, denoted by* $D_{(n_\theta,n_\phi)}$*, from the rectangular panel in* (a). (c) *is the transformed triangular patch* $\tilde{D}_{(n_\theta,n_\phi)}$. (d) *shows the quadrature nodes (red) on integration contour* $\partial\tilde{D}_{(n_\theta,n_\phi)}$*, the boundary of the transformed triangular patch.*

$c^{(1,1)} = \mu(\boldsymbol{r}^{(1,1)})$ is known, and there are only $(p^2+p)/2-1$ quaternionic unknowns (and corresponding equations).

We are now ready to substitute the density approximated as in (21) into the DLP (10). However, the double-layer kernel needs to be written in quaternionic form to take advantage of Corollary 3.4. The following lemma summarizes the result.

LEMMA 3.7. *Let* r *and* n_r *be the source location and the normal on* D*, respectively, in quaternionic form:*

$$r = 0 + x\boldsymbol{i} + y\boldsymbol{j} + z\boldsymbol{k}, \;\; n_r = 0 + n_1\boldsymbol{i} + n_2\boldsymbol{j} + n_3\boldsymbol{k}. \tag{22}$$

If the density is approximated as in (21)*, then the scalar part of*

$$-\int_D \frac{(r'-r)n_r}{4\pi|r'-r|^3}\left(\sum_{k=1}^{p}\sum_{l=1}^{k} f^{(k,l)}(\boldsymbol{r})c^{(k,l)}\right) dS_{\boldsymbol{r}} \tag{23}$$

is a pth-order convergent scheme to the DLP defined on D*.*

Proof. The proof follows from the following two observations: (i) owing to (21), only the scalar part of $\sum_{k=1}^{p}\sum_{l=1}^{k} f^{(k,l)}c^{(k,l)}$ remains and (ii) the scalar part of quaternion product rn_r is given by $-\boldsymbol{r}\cdot\boldsymbol{n_r}$. ∎

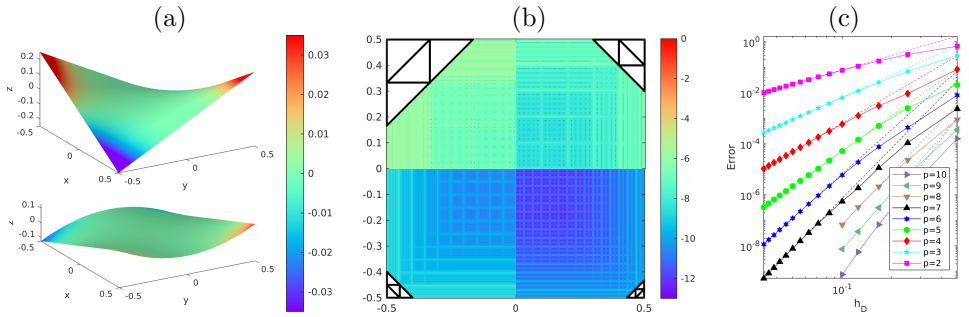

FIG. 3. (a): *Two examples of the function pairs* (z, μ) *constructed using the procedure outlined in section* 5.1. *In each case, the* $z-$*component is plotted with color scaled by the density* μ. (b): *The density approximation scheme* (21) *is applied to each of these function pairs, and the max of the relative* L^∞ *error is plotted here. The domain in* (x, y) *is subdivided in the manner shown here:* $h_D = 1/6, 1/10, 1/20, 1/30$. *The four skeletons on the corners illustrate refinements of the triangular grids at four corresponding quadrants.* (c): *Convergence plot of approximation error using* $p = 2, \ldots, 7$. *Dashed lines of corresponding colors are plots of expected error. For* $p > 7$, *the generalized higher-order approximation scheme in* (24) *was employed.*

Finally, to construct basis functions up to an arbitrary order beyond $p = 7$, we can exploit the fact that restricting harmonic polynomials to a unit sphere yields the standard spherical harmonics [8]. Similar to (19), we can chose p of the $2p + 1$ solid spherical harmonics of degree p. For example, let (ρ, θ, ϕ) be the coordinates of a point in spherical coordinates; then, we can set

$$\mathcal{P}_p = \{\rho^p \cos(k\phi) P_p^k(\cos\theta),\ k = 1, \ldots, p\}, \tag{24}$$

where $P_p^k(\cos\theta) = (-1)^k \sin^k\theta \frac{d^k}{d(\cos\theta)^k}\left(P_p(\cos\theta)\right)$ are the associated Legendre polynomials. When these functions are expressed in terms of the Cartesian coordinates, $x = \rho\sin\theta\cos\phi, y = \rho\sin\theta\sin\phi$, and $z = \rho\cos\theta$, we get a set of homogeneous harmonic polynomials of degree p. For example, consider the case of $p = 8$, $k = 2$; we get the following after using basic trigonometric identities:

(25)

$$\begin{aligned}\rho^8\cos(2\phi)P_8^2(\cos\theta) &= \frac{315}{16}\rho^8\cos(2\phi)\sin^2\theta\left(143\cos^6\theta - 143\cos^4\theta + 33\cos^2\theta - 1\right)\\ &= \frac{315}{16}\left(x^2 - y^2\right)\left(143z^6 - 143z^4(x^2+y^2+z^2) + 33z^2(x^2+y^2+z^2)^2\right.\\ &\qquad\left. - (x^2+y^2+z^2)^3\right).\end{aligned}$$

The convergence results of the approximation using this basis up to order 10 are shown in Figure 3.

4. Numerical scheme. We now have all the tools necessary to build a high-order accurate close evaluation scheme. Here, we will restrict our discussion to toroidal geometries parameterized by an infinitely differentiable, doubly periodic function $\boldsymbol{r}(\theta, \phi) = (x(\theta, \phi), y(\theta, \phi), z(\theta, \phi))$, where $(\theta, \phi) \in [0, 2\pi)^2$, with the understanding that the scheme can be generalized to other topologies and problem settings (since it inherently works at the level of local patches). Such a surface can be covered by the images of the disjoint union of uniform rectangular patches in parameter space as shown in Figure 2(a). When target $\boldsymbol{r}'$ is far from $\mathcal{M}$, we simply use the standard

Nyström discretization for evaluation of (1) based on a composite tensor-product Gauss–Legendre quadrature (e.g., see [4]).

For a given quadrature patch D, let $L(D) = \sqrt{\int_D dS_{\boldsymbol{r}}}$ be the characteristic length [18, sect. 3.1] measuring the dimension of a typical patch D. We define the close field cutoff to be $|\boldsymbol{r}' - \boldsymbol{c}(D)| \leq \lambda L(D)$, where $\boldsymbol{c}(D)$ is the centroid of patch D, λ is a set parameter via heuristic screening, and target $\boldsymbol{r}'$ could be off-surface or from neighboring patches (see [9, sect. 4.1] for details).

For both weakly singular and nearly singular integrals, our numerical scheme essentially remains the same. Therefore, from here on, we do not distinguish whether the target is on or off the surface. A high-level schematic description of the scheme is given in Figure 2(b–d). In a patch D, where the DLP is singular, we reduce the 2-form integration to 1-form integration on ∂D. The steps involved in this conversion are described next.

4.1. Close evaluation scheme for Laplace DLPs. The computation proceeds in two stages. In the first stage, which is *target-independent*, the density function is expressed in terms of the quaternionic basis functions $\{\nabla \mathcal{P}_k\}$. In the second stage, which is *target-dependent*, a sequence of steps are outlined that accomplish 2-form to 1-form conversion of the DLP.

Stage 1*: Precomputation.* Given the spatial discretization parameters, n_θ and n_ϕ, we cover $\mathcal{M}$ with n_θ-by-n_ϕ rectangular patches, with a composite p-by-p Gauss–Legendre quadrature on each patch as shown in Figure 2(a). On a standard patch, we further divide it into two triangular patches as shown in Figure 2(a). For each triangular patch D, we first identify the set of all close targets. A coordinate transform is applied on each such target $\boldsymbol{r}'$ and the sources in D such that $\boldsymbol{r}^{(1,1)}$ becomes the origin (Figure 2(c)). Points after transformation are denoted as $\tilde{\boldsymbol{r}}'$ and $\tilde{\boldsymbol{r}}^{(k,l)}$, $1 \leq l \leq k \leq p$.

Enforcing (21) in the transformed coordinate system at the rest of the quadrature nodes, we obtain the following system of vector equations:

$$\sum_{k=2}^{p} \sum_{l=1}^{k} A[f^{(k,l)}](\tilde{\boldsymbol{r}}^{(i,j)}) C^{(k,l)} = U^{(i,j)}, \quad 1 \leq j \leq i,\ 1 < i \leq p, \tag{26}$$

where the operator $A[\cdot]$ acting on a quaternionic function f, the unknown coefficient vector C, and the right-hand side vector U are given by

(27)

$$A[f] = \begin{pmatrix} 0 & -f_1 & -f_2 & -f_3 \\ f_1 & 0 & -f_3 & f_2 \\ f_2 & f_3 & 0 & -f_1 \\ f_3 & -f_2 & f_1 & 0 \end{pmatrix}, \; C^{(k,l)} = \begin{pmatrix} c_0 \\ c_1 \\ c_2 \\ c_3 \end{pmatrix}^{(k,l)}, \text{and } U^{(i,j)} = \begin{pmatrix} \mu(\boldsymbol{r}^{(i,j)}) - \mu(\boldsymbol{r}^{(1,1)}) \\ 0 \\ 0 \\ 0 \end{pmatrix}.$$

Assembling the vector equations (26) for all (i, j) yields a square linear system of size $4 \cdot (\frac{p(p+1)}{2} - 1)$ for which we simply apply a direct solver. Therefore, this stage incurs a computational cost of $\mathcal{O}(p^6)$ per triangular patch D.

Stage 2*:* 2*-to-*1 *form conversion and contour integration.* Once the quaternionic coefficients $c^{(k,l)}$ for approximating the density are found in Stage 1, the next step is to substitute them in (23) and proceed with converting this 2-form to quaternionic differential 1-form $\omega^{(k,l)}$ using Lemma 3.3. After the coordinate transformation, we can rewrite (23) as (we omit $\tilde{}$ on $\tilde{\boldsymbol{r}}$)

$$\sum_{k=2}^{p}\sum_{l=1}^{k}\left(\frac{1}{4\pi}\int_{\tilde{D}}\alpha^{(k,l)}\right)c^{(k,l)}+\frac{1}{4\pi}\int_{\tilde{D}}\alpha^{(1,1)}\mu(\boldsymbol{r}^{(1,1)}), \tag{28}$$
$$\text{where}\quad \alpha^{(k,l)}=-\frac{(r'-r)n_r}{|r'-r|^3}\,f^{(k,l)}\,dS_{\boldsymbol{r}}.$$

The quaternionic components of $\alpha^{(k,l)}$ can be simplified to the following after carrying out the product of quaternions on the right-hand side:

$$\alpha_i^{(k,l)}=\frac{1}{|\boldsymbol{r'}-\boldsymbol{r}|^3}\boldsymbol{q}_i^{(k,l)}\ldots\boldsymbol{n_r}\,dS_{\boldsymbol{r}},\ k=2,\ldots,p,\ 1\le l\le k, \tag{29}$$

where $i=0,1,2,3$ corresponds is the index of the quaternion and each of the vectors $\boldsymbol{q}_i^{(k,l)}$ are kth degree polynomials in $\boldsymbol{r}$, which can be derived using the quaternion product as

(30)
$$\begin{aligned}
\boldsymbol{q}_0^{(k,l)}(\boldsymbol{r'},\boldsymbol{r})&=\boldsymbol{f}^{(k,l)}(\boldsymbol{r})\times(\boldsymbol{r'}-\boldsymbol{r}),\\
\boldsymbol{q}_1^{(k,l)}(\boldsymbol{r'},\boldsymbol{r})&=-\Big((\boldsymbol{r'}-\boldsymbol{r})\cdot\boldsymbol{f}^{(k,l)}(\boldsymbol{r})\Big)\boldsymbol{e}_1+(x'-x)\,\boldsymbol{f}^{(k,l)}(\boldsymbol{r})+f_1^{(k,l)}(\boldsymbol{r})\,(\boldsymbol{r'}-\boldsymbol{r}),\\
\boldsymbol{q}_2^{(k,l)}(\boldsymbol{r'},\boldsymbol{r})&=-\Big((\boldsymbol{r'}-\boldsymbol{r})\cdot\boldsymbol{f}^{(k,l)}(\boldsymbol{r})\Big)\boldsymbol{e}_2+(y'-y)\,\boldsymbol{f}^{(k,l)}(\boldsymbol{r})+f_2^{(k,l)}(\boldsymbol{r})\,(\boldsymbol{r'}-\boldsymbol{r}),\\
\boldsymbol{q}_3^{(k,l)}(\boldsymbol{r'},\boldsymbol{r})&=-\Big((\boldsymbol{r'}-\boldsymbol{r})\cdot\boldsymbol{f}^{(k,l)}(\boldsymbol{r})\Big)\boldsymbol{e}_3+(z'-z)\,\boldsymbol{f}^{(k,l)}(\boldsymbol{r})+f_3^{(k,l)}(\boldsymbol{r})\,(\boldsymbol{r'}-\boldsymbol{r}).
\end{aligned}$$

The advantage of our density approximation scheme is now apparent: from (29), it is clear that $\alpha_i^{(k,l)}$ is an exact form by construction, and we can apply Lemma 3.3 to convert it into a 1-form $\omega_i^{(k,l)}$ as follows:

$$\begin{aligned}
\omega_i^{(k,l)}=&\left(\int_0^1\frac{tzq_{i,2}^{(k,l)}(\boldsymbol{r'},t\boldsymbol{r})-tyq_{i,3}^{(k,l)}(\boldsymbol{r'},t\boldsymbol{r})}{|t\boldsymbol{r}-\boldsymbol{r'}|^3}dt\right)dx\\
&+\left(\int_0^1\frac{txq_{i,3}^{(k,l)}(\boldsymbol{r'},t\boldsymbol{r})-tzq_{i,1}^{(k,l)}(\boldsymbol{r'},t\boldsymbol{r})}{|t\boldsymbol{r}-\boldsymbol{r'}|^3}dt\right)dy\\
&+\left(\int_0^1\frac{tyq_{i,1}^{(k,l)}(\boldsymbol{r'},t\boldsymbol{r})-txq_{i,2}^{(k,l)}(\boldsymbol{r'},t\boldsymbol{r})}{|t\boldsymbol{r}-\boldsymbol{r'}|^3}dt\right)dz.
\end{aligned} \tag{31}$$

Notice that the numerators of each of the integrands in the 1-form above are polynomials of degree $(k+1)$ in the variable t. Defining $M_k(\boldsymbol{r'},\boldsymbol{r})=\int_0^1\frac{t^k}{|t\boldsymbol{r}-\boldsymbol{r'}|^3}dt$ and using (30), we can separate out the terms that depend on t and rewrite $\omega_i^{(k,l)}$ as

(32)
$$\begin{aligned}
\omega_i^{(k,l)}=&\Big(v_{i,1}^{(k,l)}(\boldsymbol{r})M_{k+1}+w_{i,1}^{(k,l)}(\boldsymbol{r'},\boldsymbol{r})M_k\Big)\,dx+\Big(v_{i,2}^{(k,l)}(\boldsymbol{r})M_{k+1}+w_{i,2}^{(k,l)}(\boldsymbol{r'},\boldsymbol{r})M_k\Big)\,dy\\
&+\Big(v_{i,3}^{(k,l)}(\boldsymbol{r})M_{k+1}+w_{i,3}^{(k,l)}(\boldsymbol{r'},\boldsymbol{r})M_k\Big)\,dz,
\end{aligned}$$

where, for brevity, we omitted $(\boldsymbol{r'},\boldsymbol{r})$ dependency on M_k. Here, $v_{i,j}^{(k,l)}(\boldsymbol{r})$ are $(k+1)$th degree polynomials in $\boldsymbol{r}$, and $w_{i,j}^{(k,l)}(\boldsymbol{r'},\boldsymbol{r})$ are kth degree polynomials in $\boldsymbol{r}$ and linear in $\boldsymbol{r'}$. The explicit expressions for these can be easily derived from (30) and (31); for

example, in the case of $i = 0$, we have

$$
\begin{aligned}
v_{0,1}^{(k,l)}(\boldsymbol{r}) &= \left(y^2+z^2\right) f_1^{(k,l)}(\boldsymbol{r}) - xy f_2^{(k,l)}(\boldsymbol{r}) - xz f_3^{(k,l)}(\boldsymbol{r}),\\
w_{0,1}^{(k,l)}(\boldsymbol{r}',\boldsymbol{r}) &= -\left(y'y+z'z\right) f_1^{(k,l)}(\boldsymbol{r}) + x'y f_2^{(k,l)}(\boldsymbol{r}) + x'z f_3^{(k,l)}(\boldsymbol{r}),\\
v_{0,2}^{(k,l)}(\boldsymbol{r}) &= -xy f_1^{(k,l)}(\boldsymbol{r}) + \left(x^2+z^2\right) f_2^{(k,l)}(\boldsymbol{r}) - yz f_3^{(k,l)}(\boldsymbol{r}),\\
w_{0,2}^{(k,l)}(\boldsymbol{r}',\boldsymbol{r}) &= y'x f_1^{(k,l)}(\boldsymbol{r}) - \left(x'x+z'z\right) f_2^{(k,l)}(\boldsymbol{r}) - y'z f_3^{(k,l)}(\boldsymbol{r}),\\
v_{0,3}^{(k,l)}(\boldsymbol{r}) &= -xz f_1^{(k,l)}(\boldsymbol{r}) - yz f_2^{(k,l)}(\boldsymbol{r}) + \left(x^2+y^2\right) f_3^{(k,l)}(\boldsymbol{r}),\\
w_{0,3}^{(k,l)}(\boldsymbol{r}',\boldsymbol{r}) &= z'x f_1^{(k,l)}(\boldsymbol{r}) + z'y f_2^{(k,l)}(\boldsymbol{r}) - \left(x'x+y'y\right) f_3^{(k,l)}(\boldsymbol{r}).
\end{aligned}
\tag{33}
$$

Also see Appendix C, where we derive explicit formulas for all the quantities $\omega_i^{(k,l)}$, $v_{i,j}^{(k,l)}$, and $w_{i,j}^{(k,l)}$ in the case of a second-order scheme.

Therefore, the kernel singularity in the DLP is now encoded into the moments $\{M_k\}$. For each source $\boldsymbol{r}$ and target $\boldsymbol{r}'$, we evaluate these moments analytically via recurrences given in Appendix B. Now, we can express the complete 1-form ω as a linear combination of each individual 1-forms with coefficients $C^{(k,l)}$ and the constant term corresponding to $k = 1$ as

$$
\omega = \mu(\boldsymbol{r}^{(1,1)})\omega_0^{(1,1)} + \sum_{k=2}^{p}\sum_{l=1}^{k} \Omega^{(k,l)} C^{(k,l)},
\tag{34}
$$

where $\Omega^{(k,l)} = [\omega_0^{(k,l)}, \omega_1^{(k,l)}, \omega_2^{(k,l)}, \omega_3^{(k,l)}]$. Then, we evaluate boundary path integral $\int_{\partial\tilde{D}} \omega$ using a high-order smooth quadrature rule (Gauss–Legendre). However, note that the 1-forms (32) are still singular if $\boldsymbol{r}'$ approaches $\boldsymbol{r}$ (as can be inferred from the base conditions (45)). But since the sources now reside on ∂D, this situation can be avoided altogether by simply choosing a larger patch on a smoothly parametrized manifold $\mathcal{M}$.

The computational complexity of this stage is primarily dictated by the evaluation of the moments $\{M_k\}$. For each target, evaluating the recurrences for these moments takes $\mathcal{O}(p)$ time for each of the $\mathcal{O}(p)$ sources on ∂D, bringing the total per target cost to $\mathcal{O}(p^2)$. Therefore, the computational cost of both stages of the close evaluation per patch D is $\mathcal{O}(p^6 + n_{targ}p^2)$, where n_{targ} is the number of targets that are considered to be close to D.

4.2. A generalization to evaluate the single-layer and the gradient of double-layer Laplace potentials. In several applications, one needs to evaluate high-order derivatives of layer potentials either as a postprocessing step or, in some cases, as part of representing the solution itself. Lemma 3.4 simplifies this task for us since we can exploit the fact that the kernels themselves are harmonic functions. For example, assuming the density is approximated as in (21), it is easy to show that the scalar part of the integral

$$
\begin{aligned}
-\int_{\mathcal{M}} \frac{1}{|r'-r|^3} \Bigg(&\left(\delta_{1j} - 3\frac{(x'-x)(r'-r)}{|r'-r|^2}\right) n_r,\ \left(\delta_{2j} - 3\frac{(y'-y)(r'-r)}{|r'-r|^2}\right) n_r,\\
&\left(\delta_{3j} - 3\frac{(z'-z)(r'-r)}{|r'-r|^2}\right) n_r \Bigg) \left(\sum_{k=1}^{p}\sum_{l=1}^{k} f^{(k,l)}(\boldsymbol{r}) c^{(k,l)}\right) dS_{\boldsymbol{r}}
\end{aligned}
\tag{35}
$$

is an approximation to $\nabla\mathcal{D}(\mu)(\boldsymbol{r})$. The requirements $d\alpha = 0$ for converting the directional derivatives of the DLP to 1-form ω are satisfied based on the interchangeability

of partial derivatives and exterior derivatives. However, constructing the 1-forms in this case also requires us to evaluate integrals of the form $L_k(\boldsymbol{r}', \boldsymbol{r}) = \int_0^1 \frac{t^k}{|t\boldsymbol{r}-\boldsymbol{r}'|^5} dt$; recurrences to evaluate these are provided in Appendix B.

Lastly, we consider the single-layer potential (SLP), given by $\mathcal{S}[\mu](\boldsymbol{r}') = \int_{\mathcal{M}} \frac{1}{|\boldsymbol{r}'-\boldsymbol{r}|}\mu(\boldsymbol{r})\, dS_{\boldsymbol{r}}$. Since the SLP does not have a 2-form structure like the DLP as in (12), we instead write it as

$$\mathcal{S}[\mu](\boldsymbol{r}') = \int_{\mathcal{M}} \frac{(r'-r)\, n_r}{|r'-r|^3} \overline{n}_r \overline{(r'-r)} \mu(\boldsymbol{r})\, dS_{\boldsymbol{r}}, \tag{36}$$

using quaternion algebra. Now, we can treat it the same way as a DLP but with a modified density function. That is, we construct the approximation

$$\overline{n}_r \overline{(r'-r)} \mu(\boldsymbol{r}) \approx \sum_{k=1}^{p} \sum_{l=1}^{k} f^{(k,l)}(\boldsymbol{r})\, c^{(k,l)}, \tag{37}$$

substitute in (36), and follow the close evaluation scheme as in section 4.1. While it appears like this approach requires us to perform the approximation (37) independently for each target since the term $\overline{(r'-r)}$ is separable, we can just form it once per patch with minor bookkeeping.

5. Numerical results and discussion. In this section, we present numerical results from a series of tests to validate the accuracy of our close evaluation scheme using a MATLAB implementation. We consider three different geometries of toroidal and spherical topologies. First, we conduct a convergence test of the quaternionic approximation algorithm presented in section 3.2. We then test the performance of our DLP close evaluation, first *via* self-convergence on three different geometries, followed by a boundary value problem solve, whose exact solution is known analytically.

5.1. Convergence properties of the quaternionic approximation. Consider a local patch D and a smooth function μ defined on it. We can express the coordinate functions of D and μ in terms of the tensor-product monic polynomials:

$$\boldsymbol{r} \approx [x, y, z]^T = [x, y, \sum_{1 \le k+l \le m} a^D_{k,l} x^k y^l]^T, \quad \mu(\boldsymbol{r}) \approx \sum_{1 \le k'+l' \le m} a^{\mu}_{k',l'} x^{k'} y^{l'}, \tag{38}$$

where $a^D_{k,l}$ and $a^{\mu}_{k',l'}$ are the Taylor coefficients of the $z-$component and μ, respectively, in terms of x and y.

In this test, we provide empirical evidence that the quaternionic approximation scheme employed in (21) is pth-order convergent. To do so, we proceed as follows. In the domain $(x, y) \in [-0.5, 0.5]^2$, we generate a sequence of the function pairs (z, μ) by setting $a^D_{k,l} = a^{\mu}_{k',l'} = 1$ and the rest to zero for each admissible pair of indices (i.e., such that $1 \le k + l \le m$ and $1 \le k' + l' \le m$). Two such pairs are plotted in Figure 3(a). Then, on each of these pairs, we construct the density approximation in quaternionic form (21) *via* collocation by solving (26). We report the relative L^∞ error between $\mu(\boldsymbol{r})$ and $\sum_{k=1}^{p} \sum_{l=1}^{k} f^{(k,l)}(\boldsymbol{r})\, c^{(k,l)}$ measured on a 250×250 target grid for four different h_D, leg size of right triangular patches, in Figure 3(b). We observe that 9-digit accuracy is reached as we reduce h_D. Moreover, from Figure 3(c), we can see that the expected order of convergence is attained asymptotically. Though high degree quaternionic approximation involves solving an ill-conditioned system for unknown quaternionic coefficients, a backward stable linear solver in practice can produce solutions with very small residuals.

5.2. Laplace DLP evaluation test. Here, we consider the double-layer solution *ansatz* (1) for the exterior Laplace equation. We begin with a cruller surface from [4] which is parametrized by an infinitely differentiable, double 2π-periodic function $\boldsymbol{r}(\theta,\phi) : [0,2\pi)^2 \to \mathbb{R}^3$, followed by a cushion surface from [19], which has a global parametrization in spherical coordinate $\boldsymbol{r}(\theta,\phi) : [-\pi/2,\pi/2]\times[0,2\pi) \to \mathbb{R}^3$. Lastly, to demonstrate the applicability of our approach to arbitrary parameterizations, we consider an input mesh without any analytic description of the geometry.

Example 1*: "Cruller" geometry.* This example demonstrates the handling of complex geometries parameterized by doubly 2π-periodic functions. We consider a smooth, warped torus surface $\mathcal{M}$ in Cartesian coordinates given by

(39)
$$\boldsymbol{r} = \boldsymbol{r}(\theta,\phi) = \left((a + f(\theta,\phi)\cos(\theta))\cos(\phi),\ (a + f(\theta,\phi)\cos(\theta))\sin(\phi),\ f(\theta,\phi)\sin(\theta)\right),$$

where $f(\theta,\phi) = b + w_c\cos(w_n\phi + w_m\theta)$, $a = 1$, and $b = 1/2$. We test the close evaluation scheme using mean curvature H as density:

$$\mu(\theta,\phi) = H(\theta,\phi) = \frac{1}{2}\left(EN - 2FM + GL\right) / \left(EG - F^2\right), \tag{40}$$

where the fundamental forms are given by $E = \boldsymbol{r}_\phi \cdot \boldsymbol{r}_\phi$, $F = \boldsymbol{r}_\phi \cdot \boldsymbol{r}_\theta$, $G = \boldsymbol{r}_\theta \cdot \boldsymbol{r}_\theta$, $L = \boldsymbol{r}_{\phi\phi} \cdot \boldsymbol{n}$, $M = \boldsymbol{r}_{\phi\theta} \cdot \boldsymbol{n}$, $N = \boldsymbol{r}_{\theta\theta} \cdot \boldsymbol{n}$, and the normal $\boldsymbol{n} = (\boldsymbol{r}_\phi \times \boldsymbol{r}_\theta)/|\boldsymbol{r}_\phi \times \boldsymbol{r}_\theta|$.

We discretize $\mathcal{M}$ uniformly with n_θ-by-n_ϕ rectangular patches and conduct a self-convergence study with reference values computed using the close evaluation scheme with $n_\theta = 108, n_\phi = 144$. The results are shown in Table 1 and Figure 4. The errors are measured at targets located on the $\phi = \pi/2$ plane (as shown in Figure 4(a)). We note that the expected order of convergence is observed asymptotically.

Example 2*: "Cushion" geometry.* In this example, we consider the cushion surface $\mathcal{M}$ from [19] defined by

$$\mathcal{M} = \boldsymbol{r}(\theta,\phi) = \left(f(\theta,\phi)\cos(\theta)\cos(\phi),\ f(\theta,\phi)\sin(\theta)\cos(\phi),\ f(\theta,\phi)\sin(\phi)\right), \tag{41}$$

where $f(\theta,\phi) = \left(4/5 + 1/2\left(\cos(2\theta) - 1\right)\left(\cos(4\phi) - 1\right)\right)^{1/2}$. The density μ is set to the mean curvature (40). As in [19], we discretize $\mathcal{M}$ using a set of nonoverlapping patches and tensor-product grids in each patch (Figure 5, left). The DLP is evaluated on two planes, intersecting the surface at $\phi = 3\pi/16$ and $\phi = 27\pi/16$, as shown in

TABLE 1

Laplace DLP close evaluation scheme using mean curvature as prescribed density in the exterior of a smooth, warped torus surface parametrized by $(\theta,\phi) \in [0,2\pi)^2$, with $w_c = 0.065$, $w_m = 3$, and $w_n = 5$. A cross-section on the YZ-plane ($\phi = \pi/2$) is chosen to study the convergence. We report both the maximum relative error and the observed convergence rate ($\hat{p}$) across the same slice as the number of panels are increased.

	$p=3$		4		5	
$n_\theta \times n_\phi$	max E_{rel}	$\hat{p}$	max E_{rel}	$\hat{p}$	max E_{rel}	$\hat{p}$
12× 16	3.70e-02		1.25e-02		6.30e-03	
36× 48	6.72e-04	3.65	8.27e-05	4.57	6.05e-06	6.32
60× 80	4.92e-05	5.12	3.32e-06	6.30	3.36e-07	5.66
84× 112	1.79e-05	3.00	9.67e-07	3.67	4.59e-08	5.91

6		7	
max E_{rel}	$\hat{p}$	max E_{rel}	$\hat{p}$
3.68e-03		1.32e-03	
1.56e-06	7.07	2.51e-07	7.80
3.40e-08	7.50	1.35e-09	10.2
3.61e-09	6.66	9.37e-11	7.94

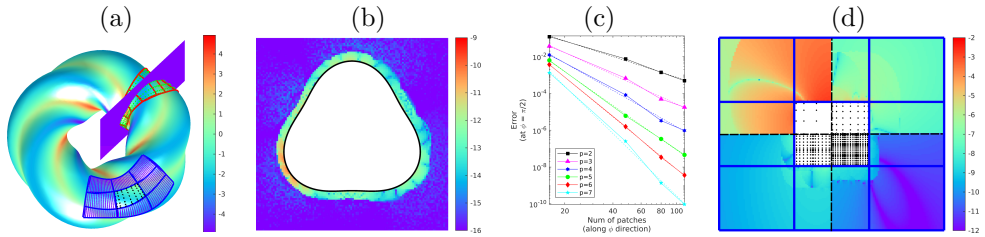

FIG. 4. *Laplace DLP close evaluation scheme on a smooth, warped torus surface, using mean curvature as prescribed density.* (a): *Surface* $\mathcal{M}$*, with* $w_c = 0.065$*,* $w_m = 3$*, and* $w_n = 5$*, showing panel divisions (red lines) intersecting* YZ*-plane and Nyström nodes (green). The color indicates the magnitude of mean curvature.* (b): *Cross-section view of the* $\log_{10}$ *relative error in the exterior of* $\mathcal{M}$ *in the* YZ*-plane* ($\phi = \pi/2$) *with* 84×112 *patches.* (c): *Rate of convergence of the relative errors across the same shown slice with respect to the number of panels along the torodial direction for* $p = 2, \ldots, 7$*.* (d): *The* $\log_{10}$ *absolute errors for on-surface targets along the surface-tangential direction. The configuration of the source patch (Nyström nodes in black) and its near neighbors on the warped torus surface is illustrated in* (a) *(blue lines). The Nyström discretization of the source patch at four corresponding quadrants are shown here.*

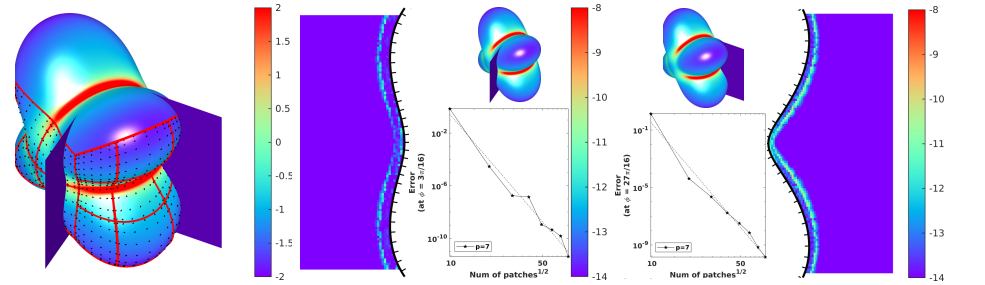

FIG. 5. *Laplace DLP close evaluation on a cushion-shaped geometry. Left: Illustration of the surface discretization with nonoverlapping patches. The magnitude of mean curvature is indicated by the color. The solution is evaluated on the shown slices. Middle: Cross-section view on the plane* $\phi = 3\pi/16$ *of the* $\log_{10}$ *relative error in the exterior of the cushion. The inset plots the relative error corresponding to* $p = 7$ *as a function of the number of patches. Max relative error is* 4.1314×10^{-12} *with a total number of* 6144 ($32 \times 32 \times 6$) *patches. Current surface discretization is shown by the ticks ("|") along the surface. Right: The* $\log_{10}$ *relative error in the exterior of the cushion on the plane* $\phi = 27\pi/16$ *with a total number of* 6144 *patches. Max relative error is* 1.4157×10^{-10}*.*

Figure 5. The relative errors are plotted as the number of patches are increased for the case of $p = 7$. While the experimental setup is slightly different from that in [19], our goal is to showcase that several more digits of accuracy can be obtained using higher-order close evaluation schemes. For example, from Figure 5, we observe that around 10 digits of accuracy (or better) can be achieved at targets that are arbitrarily close to the surface on both the planes.

Example 3*: "Bunny" geometry.* Finally, we showcase that, when a smooth surface is given without (θ, ϕ) parametrization, a local correction could still be implemented to a higher-order based on a local set of control points and a high-order polynomial interpolation. The bunny geometry is taken from a standard mesh library. We use an interactive high-quality quad remeshing tool developed in [24] to return a collection of patches and nodes within. We then construct a 6th-order polynomial approximation to each patch and generate Gauss–Legendre quadrature nodes for naive evaluation and boundaries of each patch for applying our close evaluation scheme. We use a randomly

chosen density function $\mu(x,y,z) = e^{xy} - 1 + x + \sin(x^4 + 1/2y^3) + y - 1/2y^2 + 1/5y^6 + z$ on the bunny surface. The results on one patch are shown in Figure 1 to demonstrate the performance.

5.3. Laplace BVP test. For this numerical experiment, we solve Laplace interior BVP inside two cruller (39) domains, one with higher curvature compared to the other, as shown in Figures 6 and 7. The boundary data is generated from a superposition of randomly distributed point sources located exterior to the domain; i.e., we evaluate the function $g(\boldsymbol{r}) = \sum_{j=1}^{N_s} G(\boldsymbol{r} - \boldsymbol{r}_j)h_j$, where $\boldsymbol{r} \in \mathcal{M}$, the sources $\boldsymbol{r}_j$ are located in the exterior, and the source strengths h_j are set to some random values. Starting from this boundary data, the BIE (8) can be solved for unknown density function μ. We use the quadrature scheme and BIE solver developed in [4] for this purpose. The resulting density μ for both geometries is plotted in Figure 6, left, and Figure 7, left. The numerical solution of the BVP is evaluated on the $\phi = \pi/8$ plane using our close evaluation scheme with $p = 7$. It is then compared against the exact solution $u_{\text{exact}}(\boldsymbol{r}') = \sum_{j=1}^{N_s} G(\boldsymbol{r}' - \boldsymbol{r}_j)h_j$, where $\boldsymbol{r}' \in \mathbb{D}$. We can make the following observations from Figures 6 and 7: (i) the accuracy is uniform throughout the interior (that is, no degradation at targets close to the boundary); (ii) similar to

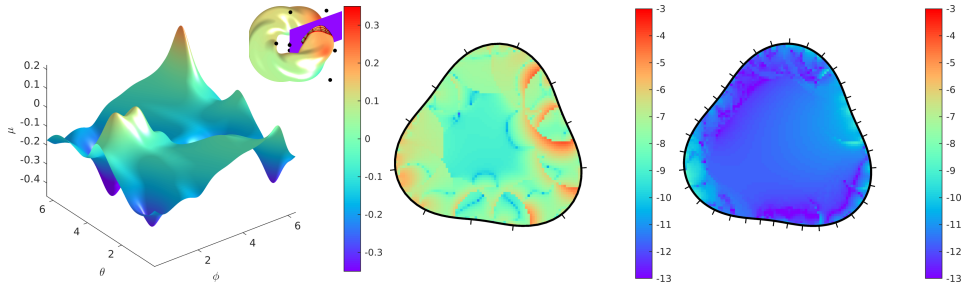

FIG. 6. *Solution of Laplace BVP in the interior of a torus, using an indirect DLP formulation* (8). *Left: Density function plotted as a function of torodial and poloidal directions. The inset at the upper right corner shows the geometry whose surface color indicates the Dirichlet data due to a few randomly placed sources (black dots) in the exterior. The solution is evaluated on the shown slice. Here the shape parameters in* (39) *were set to* $w_c = 0.065$, $w_m = 3$, *and* $w_n = 5$. *Middle: Cross-section view of the* $\log_{10}$ *relative error on the plane* $\phi = \pi/8$. *Max relative error is* 7.1761×10^{-5} *with* 12×16 *panels. Right: The* $\log_{10}$ *relative error on the same shown slice with* 36×48 *panels. Max relative error is* 3.7405×10^{-9}.

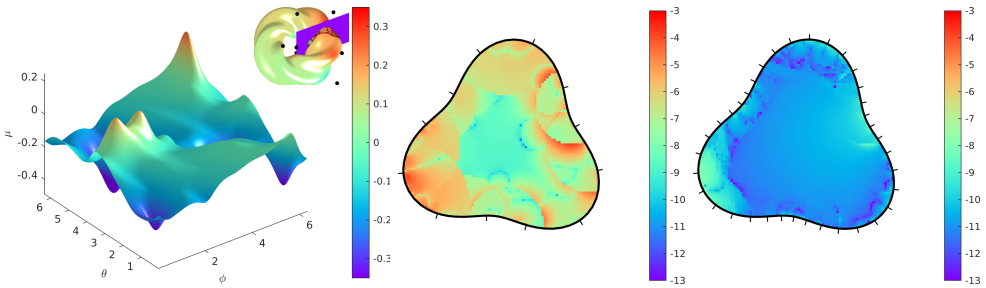

FIG. 7. *Same setup as in Figure* 6 *but with shape parameters* $w_c = 0.1$, $w_m = 3$, *and* $w_n = 5$ *(higher curvature). The max relative error is* 1.6098×10^{-4} *with* 12×16 *panels (middle), and with* 36×48 *panels, it is* 1.6667×10^{-8} *(right).*

the exterior problem case, order of convergence is consistent with the basis function space used; and (iii) level of accuracy achieved is consistent with the complexity of the geometry.

6. Conclusions. In summary, we presented a high-order technique for evaluating nearly singular integrals for Laplace layer potentials in three dimensions and demonstrated its efficacy on a range of test problems. This scheme has modest requirements: it can work on any user-supplied surface mesh directly to solve the close evaluation problem up to the level of accuracy commensurate with that of the given data. Moreover, to some extent, this scheme is *dimension-agnostic*. It is intriguing to note that if we carry out the same steps for two-dimensional DLPs, we will recover the scheme of Helsing and Ojala [13] (see [35, sect. 8.1] for further details). There, nearly singular integrals were computed using a quadrature scheme that employs piecewise complex monomial approximation on panels, Cauchy's theorem, and recurrence relations. In our case, we can use harmonic polynomials in two dimensions—which are closely related to complex monomials—for density approximation, and the DLP can be transformed from a 1-form line integral to a 0-form antiderivative evaluation (i.e., using (13) and (14)).

We plan to extend our work on several fronts. Our immediate next step is to integrate the close evaluation routine with an open-source fast multipole method package (e.g., [9]) and test its performance on large-scale examples. Another natural direction is to consider various other elliptic PDE kernels including Helmholtz, Stokes, and Navier kernels. As indicated earlier, such a task is nontrivial since the density approximation likely needs to be modified and new recurrences for 1-forms need to be derived. Lastly, accurate three-dimensional close evaluation schemes open up possibilities to investigate physical phenomena that are otherwise hard to simulate including chain formation and chaotic behavior in vesicle electrohydrodynamics [28, 31], flows through complex geometries [17, 32], and self-assembly of active particles [33, 15]. We plan to generalize these previous works to large-scale three-dimensional flows with arbitrary particle shapes.

Appendix A. Proof of Lemma 3.3.

Proof. Denoting $P(\boldsymbol{r}) = \int_0^1 (tzg_2(t\boldsymbol{r}) - tyg_3(t\boldsymbol{r}))\,dt$, $Q(\boldsymbol{r}) = \int_0^1 (txg_3(t\boldsymbol{r}) - tzg_1(t\boldsymbol{r}))dt$, and $R(\boldsymbol{r}) = \int_0^1 (tyg_1(t\boldsymbol{r}) - txg_2(t\boldsymbol{r}))\,dt$, the exterior derivative of (16), $\omega = P(\boldsymbol{r})dx + Q(\boldsymbol{r})dy + R(\boldsymbol{r})dz$, is

$$d\omega = \left(\frac{\partial R}{\partial y} - \frac{\partial Q}{\partial z}\right) dy \wedge dz + \left(\frac{\partial P}{\partial z} - \frac{\partial R}{\partial x}\right) dz \wedge dx + \left(\frac{\partial Q}{\partial x} - \frac{\partial P}{\partial y}\right) dx \wedge dy. \tag{42}$$

The first term, $\frac{\partial R}{\partial y} - \frac{\partial Q}{\partial z}$, can be expanded as

$$\begin{aligned}&\frac{\partial}{\partial y}\left(\int_0^1 (tyg_1(t\boldsymbol{r}) - txg_2(t\boldsymbol{r}))\,dt\right) - \frac{\partial}{\partial z}\left(\int_0^1 (txg_3(t\boldsymbol{r}) - tzg_1(t\boldsymbol{r}))\,dt\right)\\ &\quad = \int_0^1 \left(tg_1(t\boldsymbol{r}) + t^2 yg_{1,y}(t\boldsymbol{r}) - t^2 xg_{2,y}(t\boldsymbol{r})\right) dt\end{aligned}$$

$$
\begin{aligned}
&- \int_0^1 \left(t^2 x g_{3,z}(t\boldsymbol{r}) - t g_1(t\boldsymbol{r}) - t^2 z g_{1,z}(t\boldsymbol{r})\right) dt \\
&= \int_0^1 \left(2t g_1(t\boldsymbol{r}) + t^2 y g_{1,y}(t\boldsymbol{r}) + t^2 z g_{1,z}(t\boldsymbol{r}) - t^2 x \left(g_{2,y}(t\boldsymbol{r}) + g_{3,z}(t\boldsymbol{r})\right)\right) dt \\
&= \int_0^1 \left(2t g_1(t\boldsymbol{r}) + t^2 y g_{1,y}(t\boldsymbol{r}) + t^2 z g_{1,z}(t\boldsymbol{r}) + t^2 x g_{1,x}(t\boldsymbol{r})\right) dt \qquad (\text{since} \quad \nabla \cdot \boldsymbol{g} = 0) \\
&= \int_0^1 \frac{d}{dt}(t^2 g_1(t\boldsymbol{r}))dt \; = g_1(\boldsymbol{r}).
\end{aligned}
$$

Treating the other two terms, $\frac{\partial P}{\partial z} - \frac{\partial R}{\partial x}$ and $\frac{\partial Q}{\partial x} - \frac{\partial P}{\partial y}$, similarly, we get the result $d\omega = g_1 dy \wedge dz + g_2 dz \wedge dx + g_3 dx \wedge dy$. ∎

Appendix B. Recurrence relations for evaluating moments. Here, we present recurrence relations for evaluating moments of high-order monic polynomials with respect to certain kernels that arise in 1-form construction. Together with M_k that is required in (32), we need L_k and N_k, defined below, for evaluating other Laplace layer potentials:

$$
\begin{aligned}
&L_k(\boldsymbol{r}', \boldsymbol{r}) = \int_0^1 \frac{t^k}{|t\boldsymbol{r} - \boldsymbol{r}'|^5} dt, \quad M_k(\boldsymbol{r}', \boldsymbol{r}) = \int_0^1 \frac{t^k}{|t\boldsymbol{r} - \boldsymbol{r}'|^3} dt, \\
&N_k(\boldsymbol{r}', \boldsymbol{r}) = \int_0^1 \frac{t^k}{|t\boldsymbol{r} - \boldsymbol{r}'|} dt.
\end{aligned} \tag{43}
$$

Using integration by parts and after some algebra, we can arrive at the following recurrences for evaluating the above moments:

$$
\begin{cases}
L_k = \frac{2\boldsymbol{r}'\cdot\boldsymbol{r}}{|\boldsymbol{r}|^2} L_{k-1} - \frac{|\boldsymbol{r}'|^2}{|\boldsymbol{r}|^2} L_{k-2} + \frac{1}{|\boldsymbol{r}|^2} M_{k-2} \\
M_k = \frac{\boldsymbol{r}'\cdot\boldsymbol{r}}{|\boldsymbol{r}|^2} M_{k-1} + \frac{k-1}{|\boldsymbol{r}|^2} N_{k-2} - \frac{1}{|\boldsymbol{r}|^2} \frac{t^{k-1}}{|t\boldsymbol{r}-\boldsymbol{r}'|}\Big|_0^1 \\
N_k = \frac{2k-1}{k} \frac{\boldsymbol{r}'\cdot\boldsymbol{r}}{|\boldsymbol{r}|^2} N_{k-1} - \frac{k-1}{k} \frac{|\boldsymbol{r}'|^2}{|\boldsymbol{r}|^2} N_{k-2} + \frac{1}{|\boldsymbol{r}|^2} \frac{t^{k-1}|t\boldsymbol{r}-\boldsymbol{r}'|}{k}\Big|_0^1
\end{cases}. \tag{44}
$$

The base conditions for these recurrences can also easily be derived as

$$
N_0 = \frac{1}{|\boldsymbol{r}|} \left(\log\left(|\boldsymbol{r}||\boldsymbol{r}-\boldsymbol{r}'| + |\boldsymbol{r}|^2 - (\boldsymbol{r}'\cdot\boldsymbol{r})\right) - \log\left(|\boldsymbol{r}'||\boldsymbol{r}| - (\boldsymbol{r}'\cdot\boldsymbol{r})\right)\right), \tag{45}
$$

$$
N_1 = \frac{1}{|\boldsymbol{r}|^2} \left(|\boldsymbol{r}-\boldsymbol{r}'| - |\boldsymbol{r}'|\right) + \frac{(\boldsymbol{r}'\cdot\boldsymbol{r})\, N_0}{|\boldsymbol{r}|^2},
$$

$$
M_0 = \frac{|\boldsymbol{r}|}{|\boldsymbol{r}|^2|\boldsymbol{r}'|^2 - (\boldsymbol{r}'\cdot\boldsymbol{r})^2} \left(\frac{|\boldsymbol{r}|^2 - (\boldsymbol{r}'\cdot\boldsymbol{r})}{|\boldsymbol{r}||\boldsymbol{r}-\boldsymbol{r}'|} + \frac{\boldsymbol{r}'\cdot\boldsymbol{r}}{|\boldsymbol{r}||\boldsymbol{r}'|}\right),
$$

$$
M_1 = \frac{1}{(\boldsymbol{r}'\cdot\boldsymbol{r})^2 - |\boldsymbol{r}'|^2|\boldsymbol{r}|^2} \left(\frac{-\boldsymbol{r}'\cdot\boldsymbol{r} + |\boldsymbol{r}'|^2}{|\boldsymbol{r}-\boldsymbol{r}'|} - |\boldsymbol{r}'|\right),
$$

$$
L_0 = \frac{1}{\left(|\boldsymbol{r}'|^2|\boldsymbol{r}|^2 - (\boldsymbol{r}'\cdot\boldsymbol{r})^2\right)^2} \left(|\boldsymbol{r}|^2 \frac{|\boldsymbol{r}|^2 - \boldsymbol{r}'\cdot\boldsymbol{r}}{|\boldsymbol{r}-\boldsymbol{r}'|} - \frac{1}{3}\frac{\left(|\boldsymbol{r}| - \boldsymbol{r}'\cdot\boldsymbol{r}\right)^3}{|\boldsymbol{r}-\boldsymbol{r}'|^3} + |\boldsymbol{r}|^2 \frac{\boldsymbol{r}'\cdot\boldsymbol{r}}{|\boldsymbol{r}'|} - \frac{1}{3}\frac{(\boldsymbol{r}'\cdot\boldsymbol{r})^3}{|\boldsymbol{r}'|^3}\right),
$$

$$
L_1 = -\frac{1}{|\boldsymbol{r}|^2} \left(\frac{1}{3}\frac{1}{|\boldsymbol{r}-\boldsymbol{r}'|^3} - \frac{1}{3}\frac{1}{|\boldsymbol{r}'|^3}\right) + \frac{(\boldsymbol{r}'\cdot\boldsymbol{r})}{|\boldsymbol{r}|^2} L_0.
$$

Appendix C. Second-order approximation scheme for Laplace DLP. Here, we provide further details on the steps outlined in section 4.1 by considering the simpler $p = 2$ case and give explicit formulas for all the intermediate operators and functions.

Stage 1*: Precomputation.* Recall that the first step is the change of coordinates wherein $\boldsymbol{r}^{(1,1)}$ becomes the origin and the rest of the quadrature nodes are transformed accordingly. In the case of $p = 2$, there are eight unknowns, four elements each of the vectors $C^{(2,1)}$ and $C^{(2,2)}$ (defined in (27)). We can explicitly write the two vector equations obtained by applying (26) as

$$\begin{aligned} A[f^{(2,1)}](\tilde{\boldsymbol{r}}^{(2,1)})C^{(2,1)} + A[f^{(2,2)}](\tilde{\boldsymbol{r}}^{(2,1)})C^{(2,2)} &= U^{(2,1)}, \\ A[f^{(2,1)}](\tilde{\boldsymbol{r}}^{(2,2)})C^{(2,1)} + A[f^{(2,2)}](\tilde{\boldsymbol{r}}^{(2,2)})C^{(2,2)} &= U^{(2,2)}. \end{aligned} \tag{46}$$

From (27), we can expand the matrix operators as

(47)
$$A[f^{(2,1)}](\boldsymbol{r}) = \begin{pmatrix} 0 & -x & 0 & z \\ x & 0 & z & 0 \\ 0 & -z & 0 & -x \\ -z & 0 & x & 0 \end{pmatrix} \quad \text{and} \quad A[f^{(2,2)}](\boldsymbol{r}) = \begin{pmatrix} 0 & 0 & -y & z \\ 0 & 0 & z & y \\ y & -z & 0 & 0 \\ -z & -y & 0 & 0 \end{pmatrix}.$$

A direct computation shows the determinant of the interpolation matrix is $|\tilde{\boldsymbol{r}}^{(2,1)} \times \tilde{\boldsymbol{r}}^{(22)}|^4 \neq 0$.

Stage 2*: 2-to-1 form conversion and contour integration.* The 1-form ω for linear case can be carried out relatively easily. We only have two quaternionic 2-forms (we omit $\tilde{}$ in $\tilde{\boldsymbol{r}}$):

(48)
$$\begin{cases} \alpha_0^{(2,1)} = \frac{(y'-y)z}{|\boldsymbol{r}'-\boldsymbol{r}|^3} dy \wedge dz + \frac{-(z'-z)x-(x'-x)z}{|\boldsymbol{r}'-\boldsymbol{r}|^3} dz \wedge dx + \frac{(y'-y)x}{|\boldsymbol{r}'-\boldsymbol{r}|^3} dx \wedge dy, \\ \alpha_1^{(2,1)} = \frac{(x'-x)x+(z'-z)z}{|\boldsymbol{r}'-\boldsymbol{r}|^3} dy \wedge dz + \frac{(y'-y)x}{|\boldsymbol{r}'-\boldsymbol{r}|^3} dz \wedge dx + \frac{(z'-z)x-(x'-x)z}{|\boldsymbol{r}'-\boldsymbol{r}|^3} dx \wedge dy, \\ \alpha_2^{(2,1)} = \frac{(y'-y)x}{|\boldsymbol{r}'-\boldsymbol{r}|^3} dy \wedge dz + \frac{(z'-z)z-(x'-x)x}{|\boldsymbol{r}'-\boldsymbol{r}|^3} dz \wedge dx + \frac{-(y'-y)z}{|\boldsymbol{r}'-\boldsymbol{r}|^3} dx \wedge dy, \\ \alpha_3^{(2,1)} = \frac{-(x'-x)z+(z'-z)x}{|\boldsymbol{r}'-\boldsymbol{r}|^3} dy \wedge dz + \frac{-(y'-y)z}{|\boldsymbol{r}'-\boldsymbol{r}|^3} dz \wedge dx + \frac{-(z'-z)z-(x'-x)x}{|\boldsymbol{r}'-\boldsymbol{r}|^3} dx \wedge dy, \end{cases}$$

(49)
$$\begin{cases} \alpha_0^{(2,2)} = \frac{(y'-y)z+(z'-z)y}{|\boldsymbol{r}'-\boldsymbol{r}|^3} dy \wedge dz + \frac{-(x'-x)z}{|\boldsymbol{r}'-\boldsymbol{r}|^3} dz \wedge dx + \frac{-(x'-x)y}{|\boldsymbol{r}'-\boldsymbol{r}|^3} dx \wedge dy, \\ \alpha_1^{(2,2)} = \frac{(z'-z)z-(y'-y)y}{|\boldsymbol{r}'-\boldsymbol{r}|^3} dy \wedge dz + \frac{(x'-x)y}{|\boldsymbol{r}'-\boldsymbol{r}|^3} dz \wedge dx + \frac{-(x'-x)z}{|\boldsymbol{r}'-\boldsymbol{r}|^3} dx \wedge dy, \\ \alpha_2^{(2,2)} = \frac{(x'-x)y}{|\boldsymbol{r}'-\boldsymbol{r}|^3} dy \wedge dz + \frac{(y'-y)y+(z'-z)z}{|\boldsymbol{r}'-\boldsymbol{r}|^3} dz \wedge dx + \frac{(z'-z)y-(y'-y)z}{|\boldsymbol{r}'-\boldsymbol{r}|^3} dx \wedge dy, \\ \alpha_3^{(2,2)} = \frac{-(x'-x)z}{|\boldsymbol{r}'-\boldsymbol{r}|^3} dy \wedge dz + \frac{-(y'-y)z+(z'-z)y}{|\boldsymbol{r}'-\boldsymbol{r}|^3} dz \wedge dx + \frac{-(z'-z)z-(y'-y)y}{|\boldsymbol{r}'-\boldsymbol{r}|^3} dx \wedge dy, \end{cases}$$

where the superscript of α denotes which basis the differential 2-form corresponds to and the subscript corresponds to the index of its quaternion pair form. Corresponding 1-forms are then given by

$$
\begin{cases}
\omega_0^{(2,1)} = & \big((xy^2+2xz^2)M_3-(y'xy+z'xz+x'z^2)M_2\big)\,dx \\
& +\big((yz^2-x^2y)M_3+(y'x^2-y'z^2)M_2\big)\,dy \\
& +\big((-2x^2z-y^2z)M_3+(z'x^2+x'xz+y'yz)\big)\,dz, \\
\omega_1^{(2,1)} = & (-xyzM_3-(z'xy-y'xz-x'yz)M_2)\,dx \\
& +\big((x^2z+z^3)M_3+(z'x^2-2x'xz-z'z^2)M_2\big)\,dy \\
& +\big(-yz^2M_3+(-y'x^2+x'xy+z'yz)M_2\big)\,dz, \\
\omega_2^{(2,1)} = & \big((x^2z-y^2z-z^3)M_3+(-x'xz+y'yz+z'z^2)M_2\big)\,dx \\
& +(2xyzM_3-2y'xzM_2)\,dy \\
& +\big((-x^3-xy^2+xz^2)M_3+(x'x^2+y'xy-z'xz)\big)\,dz, \\
\omega_3^{(2,1)} = & \big(-x^2yM_3+(x'xy+cyz-y'z^2)M_2\big)\,dx \\
& +\big((x^3+xz^2)M_3-(x'x^2+2z'xz-x'z^2)M_2\big)\,dy \\
& +(-xyzM_3+(z'xy+y'xz-x'yz)M_2)\,dz,
\end{cases}
\tag{50}
$$

$$
\begin{cases}
\omega_0^{(2,2)} = & \big((xz^2-xy^2)M_3+(x'y^2-x'z^2)M_2\big)\,dx \\
& +\big((-x^2y-2yz^2)M_3+(x'xy+z'yz+y'z^2)M_2\big)\,dy \\
& +\big((x^2z+2y^2z)M_3+(-z'y^2-x'xz-y'yz)\big)\,dz, \\
\omega_1^{(2,2)} = & (-2xyzM_3+2x'yzM_2)\,dx \\
& +\big((x^2-y^2z+z^3)M_3+(-x'xz+y'yz-z'z^2)M_2\big)\,dy \\
& +\big((x^2y+y^3-yz^2)M_3+(-x'xy-y'y^2+z'yz)M_2\big)\,dz, \\
\omega_2^{(2,2)} = & \big((-y^2z-z^3)M_3-(z'y^2-2y'yz-z'z^2)M_2\big)\,dx \\
& +(xyzM_3+(z'xy-y'xz-x'yz)M_2)\,dy \\
& +\big(xz^2M_3+(-y'xy+x'y^2-z'xz)\big)\,dz, \\
\omega_3^{(2,2)} = & \big((-y^3-yz^2)M_3+(y'y^2+2z'yz-y'z^2)M_2\big)\,dx \\
& +\big(xy^2M_3-(y'xy+z'xz-x'z^2)M_2\big)\,dy \\
& +(xyzM_3+(-z'xy+y'xz-x'yz)M_2)\,dz.
\end{cases}
\tag{51}
$$

Now we have expression for the complete 1-form ω,

$$
\omega = \mu\left(\boldsymbol{r}^{(1,1)}\right)\omega_0^{(1,1)} + \Omega^{(2,1)}C^{(2,1)} + \Omega^{(2,2)}C^{(2,2)}, \tag{52}
$$

where $\Omega^{(k,l)} = [\omega_0^{(k,l)}, \omega_1^{(k,l)}, \omega_2^{(k,l)}, \omega_3^{(k,l)}]$. Lastly, the contour integral $\int_{\partial\tilde{D}}\omega$ is evaluated on each transformed patch.

Acknowledgments. We thank Alex Barnett, Charles Epstein, Leslie Greengard, and Manas Rachh for many useful discussions pertaining to this work.

REFERENCES

[1] L. af Klinteberg and A.-K. Tornberg, *Adaptive quadrature by expansion for layer potential evaluation in two dimensions*, SIAM J. Sci. Comput., 40 (2018), pp. A1225–A1249.

[2] D. Arnold, R. Falk, and R. Winther, *Finite element exterior calculus, homological techniques, and applications*, Acta Numer., 15 (2006), pp. 1–155.

[3] A. Barnett, *Evaluation of layer potentials close to the boundary for Laplace and Helmholtz problems on analytic planar domains*, SIAM J. Sci. Comput., 36 (2014), pp. A427–A451.
[4] A. Barnett, L. Greengard, and T. Hagstrom, *High-order discretization of a stable time-domain integral equation for 3D acoustic scattering*, J. Comput. Phys., 402 (2020), p. 109047.
[5] A. Barnett, B. Wu, and S. Veerapaneni, *Spectrally accurate quadratures for evaluation of layer potentials close to the boundary for the 2D Stokes and Laplace equations*, SIAM J. Sci. Comput., 37 (2015), pp. B519–B542.
[6] J. T. Beale, W. Ying, and J. R. Wilson, *A simple method for computing singular or nearly singular integrals on closed surfaces*, Commun. Comput. Phys., 20 (2016), pp. 733–753.
[7] C. Carvalho, S. Khatri, and A. Kim, *Asymptotic analysis for close evaluation of layer potentials*, J. Comput. Phys., 355 (2018), pp. 327–341.
[8] J. Gallier, *Notes on Spherical Harmonics and Linear Representations of Lie Groups*, preprint, University of Pennsylvania, 2009.
[9] L. Greengard, M. O'Neil, M. Rachh, and F. Vico, *Fast multipole methods for the evaluation of layer potentials with locally-corrected quadratures*, J. Comput. Phys., 10 (2021), 100092.
[10] L. Greengard and V. Rokhlin, *A fast algorithm for particle simulations*, J. Comput. Phys., 73 (1987), pp. 325–348.
[11] S. Hao, A. Barnett, P.-G. Martinsson, and P. Young, *High-order accurate methods for Nyström discretization of integral equations on smooth curves in the plane*, Adv. Comput. Math., 40 (2014), pp. 245–272.
[12] J. Helsing, *A higher-order Singularity Subtraction Technique for the Discretization of Singular Integral Operators on Curved Surfaces*, preprint, arXiv:1301.7276, 2013.
[13] J. Helsing and R. Ojala, *On the evaluation of layer potentials close to their sources*, J. Comput. Phys., 227 (2008), pp. 2899–2921.
[14] A. Klöckner, A. Barnett, L. Greengard, and M. O'Neil, *Quadrature by expansion: A new method for the evaluation of layer potentials*, J. Comput. Phys., 252 (2013), pp. 332–349.
[15] R. Kohl, E. Corona, V. Cheruvu, and S. Veerapaneni, *Fast and Accurate Solvers for Simulating Janus Particle Suspensions in Stokes Flow*, preprint, arXiv:2104.14068, 2021.
[16] R. Kress, V. Maz'ya, and V. Kozlov, *Linear Integral Equations*, Appl. Math. Sci. 82, Springer, New York, 1989.
[17] G. R. Marple, A. Barnett, A. Gillman, and S. Veerapaneni, *A fast algorithm for simulating multiphase flows through periodic geometries of arbitrary shape*, SIAM J. Sci. Comput., 38 (2016), pp. B740–B772.
[18] M. J. Morse, A. Rahimian, and D. Zorin, *A robust solver for elliptic pdes in 3D complex geometries*, J. Comput. Phys., 442 (2021), 110511.
[19] C. Pérez-Arancibia, L. M. Faria, and C. Turc, *Harmonic density interpolation methods for high-order evaluation of Laplace layer potentials in 2D and 3D*, J. Comput. Phys., 376 (2019), pp. 411–434.
[20] M. Rachh, A. Klöckner, and M. O'Neil, *Fast algorithms for quadrature by expansion* I: *Globally valid expansions*, J. Comput. Phys., 345 (2017), pp. 706–731.
[21] A. Rahimian, A. Barnett, and D. Zorin, *Ubiquitous evaluation of layer potentials using quadrature by kernel-independent expansion*, BIT, 58 (2018), pp. 423–456.
[22] M. Siegel and A.-K. Tornberg, *A local target specific quadrature by expansion method for evaluation of layer potentials in 3D*, J. Comput. Phys., 364 (2018), pp. 365–392.
[23] M. Spivak, *Calculus on Manifolds: A Modern Approach to Classical Theorems of Advanced Calculus*, CRC Press, Boca Raton, FL, 2018.
[24] K. Takayama, D. Panozzo, A. Sorkine-Hornung, and O. Sorkine-Hornung, *Sketch-based generation and editing of quad meshes*, ACM Trans. Graphics, 32 (2013), pp. 1–8.
[25] S. Tlupova and J. T. Beale, *Regularized single and double layer integrals in 3D Stokes flow*, J. Comput. Phys., 386 (2019), pp. 568–584.
[26] A.-K. Tornberg and L. Greengard, *A fast multipole method for the three-dimensional Stokes equations*, J. Comput. Phys., 227 (2008), pp. 1613–1619.
[27] G. Turk and M. Levoy, *Zippered polygon meshes from range images*, in Proceedings of the 21st Annual Conference on Computer Graphics and Interactive Techniques, Association for Computing Machinery, 1994, pp. 311–318.
[28] S. Veerapaneni, *Integral equation methods for vesicle electrohydrodynamics in three dimensions*, J. Comput. Phys., 326 (2016), pp. 278–289.
[29] M. Wala and A. Klöckner, *A fast algorithm for quadrature by expansion in three dimensions*, J. Comput. Phys., 388 (2019), pp. 655–689.
[30] M. Wala and A. Klöckner, *Optimization of fast algorithms for global quadrature by expansion using target-specific expansions*, J. Comput. Phys., 403 (2020), 108976.

[31] B. Wu and S. Veerapaneni, *Electrohydrodynamics of deflated vesicles: Budding, rheology and pairwise interactions*, J. Fluid Mech., 867 (2019), pp. 334–347.
[32] B. Wu, H. Zhu, A. Barnett, and S. Veerapaneni, *Solution of Stokes flow in complex non-smooth 2D geometries via a linear-scaling high-order adaptive integral equation scheme*, J. Comput. Phys., 410 (2020), 109361.
[33] W. Yan, E. Corona, D. Malhotra, S. Veerapaneni, and M. Shelley, *A scalable computational platform for particulate Stokes suspensions*, J. Comput. Phys., 416 (2020), 109524.
[34] L. Ying, G. Biros, and D. Zorin, *A high-order 3D boundary integral equation solver for elliptic PDEs in smooth domains*, J. Comput. Phys., 219 (2006), pp. 247–275.
[35] H. Zhu, *Fast, High-Order Accurate Integral Equation Methods and Application to PDE-Constrained Optimization*, Ph.D. thesis, The University of Michigan, 2021.